Neuroglobin effectively halts vision loss in Harlequin mice at an advanced stage of optic nerve degeneration

Hélène Cwerman-Thibault, Christophe Lechauve, Vassilissa Malko-Baverel, Sébastien Augustin, Gwendoline Le Guilloux, Élodie Reboussin, Julie Degardin-Chicaud, Manuel Simonutti, Thomas Debeir, Marisol Corral-Debrinski

Neurobiology of Disease 159 (2021) 105483

Contents lists available at ScienceDirect

Neurobiology of Disease

journal homepage: www.elsevier.com/locate/ynbdi

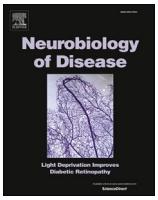

Neuroglobin effectively halts vision loss in *Harlequin* mice at an advanced stage of optic nerve degeneration

Hélène Cwerman-Thibault [b,1,2], Christophe Lechauve [a,2,3], Vassilissa Malko-Baverel [b,1], Sébastien Augustin [a], Gwendoline Le Guilloux [b,1], Élodie Reboussin [a], Julie Degardin-Chicaud [a], Manuel Simonutti [a], Thomas Debeir [c,4], Marisol Corral-Debrinski [a,*,1]

[a] *Sorbonne Université, INSERM, CNRS, Institut de la Vision, F-75012 Paris, France*
[b] *Université de Paris, NeuroDiderot, Inserm, F-75019 Paris, France*
[c] *Sanofi – Ophthalmology, F-75012 Paris, France*

A R T I C L E I N F O

Keywords:
Neuroglobin
Mitochondria
Retinal ganglion cells
Optic nerve
Gene therapy
Harlequin mice

A B S T R A C T

Mitochondrial diseases are among the most prevalent groups of inherited neurological disorders, affecting up to 1 in 5000 adults. Despite the progress achieved on the identification of gene mutations causing mitochondrial pathologies, they cannot be cured so far. *Harlequin* mice, a relevant model of mitochondrial pathology due to apoptosis inducing factor depletion, suffer from progressive disappearance of retinal ganglion cells leading to optic neuropathy. In our previous work, we showed that administering adeno-associated virus encompassing the coding sequences for neuroglobin, (a neuroprotective molecule belonging to the globin family) or apoptosis-inducing factor, before neurodegeneration onset, prevented retinal ganglion cell loss and preserved visual function.

One of the challenges to develop an effective treatment for optic neuropathies is to consider that by the time patients become aware of their handicap, a large amount of nerve fibers has already disappeared.

Gene therapy was performed *in Harlequin* mice aged between 4 and 5 months with either a neuroglobin or an apoptosis-inducing factor vector to determine whether the increased abundance of either one of these proteins in retinas could preserve visual function at this advanced stage of the disease.

We demonstrated that gene therapy, by preserving the connectivity of transduced retinal ganglion cells and optic nerve bioenergetics, results in the enhancement of visual cortex activity, ultimately rescuing visual impairment.

This study demonstrates that: (a) An increased abundance of neuroglobin functionally overcomes apoptosis-inducing factor absence in *Harlequin* mouse retinas at a late stage of neuronal degeneration; (b) The beneficial effect for visual function could be mediated by neuroglobin localization to the mitochondria, thus contributing to the maintenance of the organelle homeostasis.

Abbreviations: AAV2/2, Adeno-Associated Viral vectors, serotype 2; IRES, encephalomyocarditis virus internal ribosome entry site; *Aifm1*, *Apoptosis Inducing Factor* gene; Aif, Apoptosis Inducing Factor; Ngb, Neuroglobin; *Hq*, *Harlequin*; GFAP, Glial fibrillary acidic protein; RGC, Retinal Ganglion cell; IS, inner segments of photoreceptors; ONL, Outer nuclear layer; INL, Inner nuclear layer; OPL, Outer plexiform layer; IPL, Inner plexiform layer; ERG, Electroretinogram; F-VEP, Flash visual evoked potential; RNFL, Retinal nerve fiber layer; PLA, Proximal ligation assay; VA, Visual acuity; CytC, Cytochrome C; Vdac, Voltage-dependent anion channel.

* Corresponding author.
E-mail address: marisol.corral@inserm.fr (M. Corral-Debrinski).
[1] Present/permanent address: Université de Paris, NeuroDiderot, Inserm, F-75019 Paris, France.
[2] H. Cwerman-Thibault and C. Lechauve contributed equally to this work as first authors.
[3] Present/permanent address: Department of Hematology, St. Jude Children's Research Hospital, Memphis, Tennessee 38,105, USA.
[4] Present/permanent address: Business Development & Licencing, Sanofi Partening, 75,008 Paris, France.

https://doi.org/10.1016/j.nbd.2021.105483
Received 28 January 2021; Received in revised form 6 August 2021; Accepted 11 August 2021
Available online 14 August 2021

1. Introduction

The functional integrity of the central nervous system is based on complex mechanisms in which the mitochondria play a key role due to their involvement in a wide range of bioenergetic and biosynthetic pathways (Golpich et al., 2016). In 2015, a cross-sectional study concluded that mitochondrial diseases are among the most prevalent groups of inherited neurologic disorders, affecting up to 1 in 4300 adults in the United Kingdom (Gorman et al., 2015). Mutations in genes encoding mitochondrial proteins located in the nucleus or the organelle are responsible for neurologic disorders (Thompson et al., 2020). The deleterious consequences of these mutations result from the impairment of: (a) energy production (Fernandez-Vizarra and Zeviani, 2021); (b) intracellular Ca^{2+} homeostasis (Modesti et al., 2021); (c) fatty acid oxidation (Wanders et al., 2020); (d) regulation of reactive oxygen species and reactive nitrogen species (Singh et al., 2019); (e) organelle dynamics and quality control (Raefsky and Mattson, 2017) and (f) mitochondrial interactions with other organelles, especially the endoplasmic reticulum (Bernard-Marissal et al., 2018). To date, there is no effective treatment for neurologic disorders with mitochondrial etiology (Davison and Rahman, 2017), (Gruosso et al., 2021).

Moreover, there are correlations between mitochondrial dysfunction and the pathogenesis of neurodegenerative diseases, including Alzheimer's disease (AD), Parkinson's disease (PD), Huntington disease (HD), spinocerebellar ataxia and amyotrophic lateral sclerosis (ALS) (Chakraborty et al., 2018), (Pass et al., 2021). To date, there is no effective treatment for these devastating neurologic disorders (Davison and Rahman, 2017). Therefore, efforts are being made to find ways to lastingly preserve mitochondrial function. Examples of such approaches include the use of (a) compounds enhancing respiratory chain activity; (b) antioxidants; (c) agents that stimulate organelle biogenesis or promote the elimination of damaged ones; (d) molecules that target mitochondrial fusion or fission processes; and (e) gene therapy to correct the genetic abnormality (Russell et al., 2020; Zhang et al., 2020).

Mouse models that faithfully recapitulate the clinical features of mitochondrial diseases have been generated to decipher the mechanisms involved in the pathogenesis (Ruzzenente et al., 2016).

Harlequin (*Hq*) mice harbor a 9-kb insertion of the ecotropic leukemia provirus in the first intron of the X-linked gene *Aifm1* that encodes Apoptosis-inducing factor (Aif). This mutation results in an 80%–90% reduction in the amount of Aif, relative to that in wild-type mice (Klein et al., 2002). The depletion of the protein leads to a complex phenotype resembling human neurodegenerative diseases due to bioenergetic failure, manifested as deterioration of the retinas, optic nerves, and several cortical regions (Klein et al., 2002); (Vahsen et al., 2004). We previously demonstrated that Aif depletion in *Hq* mice results in optic atrophy and visual impairment. The loss of retinal ganglion cells (RGCs) reached up to 40% of control values in *Hq* mice from the age of 6 months (Bouaita et al., 2012); (Lechauve et al., 2014). Interestingly, an approximate 50% decrease in the steady-state levels of neuroglobin was also found in retinas from *Hq* mice relative to those of control mice (Lechauve et al., 2014).

Neuroglobin (encoded by the *Ngb* gene) was identified in 2000 as a member of the globin superfamily (Burmester et al., 2000). The protein consists of 151 amino acids and is highly abundant in the central nervous system, being present in both neurons (Hundahl et al., 2010) and astrocytes (Chen et al., 2015). The neuroprotective role of neuroglobin has been largely documented *in vitro* and *in vivo* (Ascenzi et al., 2016; Van Acker et al., 2018). We have demonstrated that, the protein localizes to mitochondria in rat retinas and that when its expression is downregulated, a defect in respiratory chain complexes I and III in optic nerves (ONs) is associated with RGC loss and visual dysfunction (Lechauve et al., 2012). We hypothesize that the neuroprotective properties of neuroglobin correlate with its ability to preserve mitochondrial function; thus, therapeutics that lead to an increase in its abundance could become a tool for managing neurologic disorders. In 1-month-old *Hq* mice, ocular gene therapy with *Aifm1* (Bouaita et al., 2012) or *Ngb* (Lechauve et al., 2014) was efficient at preventing RGC death, preserving respiratory chain complex I activity in the ONs and protecting visual function (Lechauve et al., 2014). Accordingly, we decided to perform gene therapy at a late stage of the disease to replicate the clinical situation in which the loss of vision is noticed by patients after the number of nerve fibers was by this time significantly decreased (Carelli et al., 2017). The goal of this study was to establish whether transduction of the injured neurons with *Ngb* or *Aifm1*, making more robust mitochondria within them, could durably protect visual function. Gene therapy, independently of the vector used, led to the preservation of functional and morphological characteristics of RGCs and to a substantial diminution in the extent of gliosis within retinas and ONs. In addition, the activities of respiratory chain complexes I and IV in ONs, which were compromised in *Hq* mice, were well preserved in mice treated with *Aifm1* or *Ngb*. In treated mice, residual RGCs and their axons provided increased electrical inputs to the visual cortex upon light stimulation leading to a significant preservation of visual function. Thus, we demonstrated that enhanced levels of neuroglobin, *via* gene therapy, was able to functionally overcome some of the deficiencies due to the lack of Aif in *Hq* mice at an advanced stage of the disease probably due to its presence inside the organelle. The protection of visual function in *Hq* mice, *via* its positive impact to mitochondrial robustness, allows to envisage its use for treating a broad spectrum of neurological diseases regardless of the genetic modification responsible for the symptoms.

2. Methods

2.1. Mice

The *Hq* mice originate from the C57BL/6J strain B6CBACaA$^{w\text{-}J}$/A-Pdc8^{Hq}/J, which harbors a spontaneous mutation in the *Aifm1* gene (http://jaxmice.jax.org/strain/000501.html). All hemizygous (*Hq*/Y) male mice used in this study were F2 mice bred from founders (*Hq*/X female mice with wild-type male mice) that had a mixed genetic background and were shipped from The Jackson Laboratory. Only the hemizygous (*Hq*/Y) male mice were evaluated and subjected to gene therapy; they were studied along with their male littermates from the colony. The mice were housed in a pathogen-free barrier facility with one to four animals per cage in a temperature-controlled environment, with a 12-h light/dark cycle and free access to food and water. Studies were conducted in accordance with (a) European Community Council Directive 2010/63/UR of September 22, 2010, on the protection of animals used for scientific purposes; (b) the rules on the care and use of animals in research issued by the French Ministry of Agriculture and the Veterinarian Department of Paris (permit no. DF/DF_2010_PA1000298) and the French Ministry of Research (Approval No. 5575); and (c) the ethics commissions of the University Paris 6 and the INSERM (Institut National de la Santé et de la Recherche Médicale) (Authorization No. 75–1710).

2.2. Confocal scanning laser ophthalmoscopy

A confocal scanning laser ophthalmoscope (cSLO) (Heidelberg Retina Angiograph, Heidelberg Engineering) with green laser illumination was used to examine *Hq* mice and aged-matched controls. Both eyes from approximately 60 *Hq* mice were examined longitudinally: first monthly, when the mice were aged between 1 and 4 months (before they received gene therapy) and then at 3 and 6 months after they were treated.

To monitor the nerve fiber layer and capture the whole surface of the retina at each session, we proceeded as described previously (Paques et al., 2006; Bouaita et al., 2012; Lechauve et al., 2014). Six *Hq* mice were rejected during these evaluations because they displayed corneal or lens opacities as evidenced by slit-lamp examination and confirmed with the ophthalmoscope. For eye fundus imaging, awake mice were held manually in an upright position in front of the apparatus after their

pupils had been dilated with tropicamide (a 1% solution from Ciba Vision). For each mouse, the observation session was limited to 1 min, with a break period of at least 1 min before any additional image captures that were necessary to obtain a global overview of the retina and the RNFL.

2.3. In vivo electrophysiology

Photopic (light-adapted) electroretinogram (ERG) and flash visual evoked potential (F-VEP) responses were recorded simultaneously from electrodes placed on the cornea and overlaying the visual cortex, respectively, as previously described (Cwerman-Thibault et al., 2017). For the light-adapted ERGs and the F-VEP response recordings, we followed the procedures published in 2009 (Jammoul et al., 2009) and 2015 (Makowiecki et al., 2015) respectively.

The studies were carried out with *Hq* mice subjected to intravitreal injection with either AAV2/2-*Ngb* or AAV2/2-*Aifm1* vector, up to six months post-injection. Aged-matched untreated *Hq* and control mice were also subjected to ERG and F-VEP recordings during the same period as the treated *Hq* animals.

The F-VEP procedure, as previously described (Cwerman-Thibault et al., 2017), involves subjecting mice twice to deep anesthesia for the implantation of stainless-steel screws in the visual cortices, seven days prior the electrophysiological recordings, and on the day of the experiment. Hence, after anesthesia three treated mice *Hq* (one injected with AAV2/2-*Aifm1* and two injected with AVV2/2-*Ngb*) and two untreated mice (one control and one *Hq*) died before or during the electrophysiological evaluations. Accordingly, we were able to evaluate ten *Hq* mice treated with each one of the vectors and thirteen untreated control and *Hq* mice.

The stimuli for ERGs and F-VEPs were generated and controlled by an Espion E2 system (Diagnosys LLC, Cambridge, UK) *via* a single flash stimulus delivered to the Ganzfeld dome in which each animal was lying. The responses were recorded simultaneously using different channels of the Espion E2 system. Two experimenters performed the experiments in a blinded manner. They did not know which *Hq* mice were being treated or with which vector.

2.4. Visual behavior evaluation

Optomotor tracking thresholds were measured under photopic conditions by collecting the optomotor responses of mice to rotating sinusoidal gratings (OptoMotry system, CerebralMechanics, Alberta, Canada) (Douglas et al., 2005; Prusky et al., 2004). The responses of the mice include reflexive movements of the head and neck that follow the direction of the rotation. The visual acuities of the right and left eyes are calculated separately because of the unequal sensitivities of the two eyes to pattern rotation: right and left eyes are most sensitive to counterclockwise and clockwise rotations, respectively (Douglas et al., 2005). The software by modifying the spatial frequency of the grating at 100% contrast until mice no longer move, calculates thresholds for each pattern of rotation.

Mice were subjected to the test 3–4 times (1–2 days apart) at different periods of the study. The first measurements were made in *Hq* mice aged between 1 and 4 months before vector administration. Subsequent measurements were made in treated *Hq* mice at 3 months (data not shown) and 6 months post-injection (just before euthanasia). Thirteen untreated control mice aged between 8 and 10 months were also evaluated during some of the sessions encompassing treated *Hq* mice about 6 months post-injection. From the 51 *Hq* mice subjected to gene therapy and alive during the whole length of the protocol, we excluded three mice, indeed they did not respond to the test because of the presence of lens opacities in both eyes (evidenced about three months post-injection by SLO visualization). These were one mouse treated with AAV2/2-*Aifm1* and two mice treated with AAV2/2-*Ngb*. The tests were performed by three experimenters who were blinded to the treatment of the animals and to the previous recorded data.

2.5. Adeno-associated virus vectors and their administration into the vitreous body

The AAV2/2-*Aifm1* and AAV2/2-*Ngb* vectors have been described previously (Bouaita et al., 2012; Lechauve et al., 2014). Briefly, they were obtained by cloning murine sequences in the pAAV-IRES-*hrGFP* vector (Agilent Technologies). The AAV2/2-*Ngb* vector contains the open reading frame (ORF) (453 bp), the 5′ untranslated region (UTR) (279 bp), and the 3′ UTR (895 bp) of the mouse *Ngb* mRNA variant 2 (NM_022414.2). The AAV2/2-*Aifm1* vector contains the 5′ UTR (87 bp), the entire ORF (1836 bp), and the 176-bp full-length 3′ UTR of the mouse *Aifm1* mRNA (NM_012019). The presence in each construction of the full UTR sequences guarantees mRNA stability and translation capacity (Weis et al., 2013). The expression cassettes flanked by the two inverted terminal repeats (ITRs) were packaged in AAV2 shells to ensure a high yield of RGC transduction (Hellstrom et al., 2009). Vectors were produced by the Translational Vector Core of the INSERM UMR1089 research unit at Nantes, France (http://umr1089.univ-nantes.fr). Vector administration was performed as previously described (Bouaita et al., 2012; Lechauve et al., 2014). Briefly, anesthetized *Hq* mice were injected with 2 μL of either AAV2/2-*Ngb* (2×10^9 vector genomes) or AAV2/2-*Aifm1* (5×10^8 vector genomes) in the vitreous body of one eye. The injection was made close to the superior area of the retina, avoiding structural disruption, bleeding, or lens injury. To target the disease at an advanced stage, with respect to RGC disappearance, *Hq* mice were subjected to evaluations of the eye fundus with a cSLO and their visual performance was assessed with the OptoMotry system at 1 month of age and monthly thereafter until the age of 4 months. The eye which gave the worst responses in the two tests was selected for gene therapy; the contralateral eye remained untreated (Fig. 1). For the gene therapy assays, only hemizygous (*Hq*/Y) male mice were used; they were studied along with untreated male littermates issued from the colony and which harbor the wild-type version of *Aifm1*. Overall, 52 mice were subjected to gene therapy: 28 with AAV2/2-*Ngb* and 24 with AAV2/2-*Aifm1*. One mouse injected with AAV2/2-*Ngb* died for natural causes about 2 months after vector administration, no tissues were collected from this mouse. One mouse injected with AAV2/2-*Aifm1* and two mice injected with AAV2/2-*Ngb* died before performing ERG/F-VEP recordings. Retinas and optic nerves were collected for only one mouse treated with AAV2/2-*Ngb*, which were used for histological studies. Additionally, two mice treated with AAV2/2-*Ngb* and one treated with AAV2/2-*Aifm1* developed lens opacity few months after vector administration; they were not subjected to ERG/F-VEP recordings. Table 1 illustrates the hallmarks of the mice evaluated and the choices made for administration of gene therapy vector regarding visual performance and eyes fundus imaging.

2.6. Histologic evaluations of retinas and optic nerves

Retinas and optic nerves (ONs) were collected and treated as described previously (Bouaita et al., 2012; Lechauve et al., 2014). Transverse sections of retinas and ONs were cut at a thickness of 12 μm on a cryostat (Microm HM560; Thermo Scientific) at −20 °C and mounted on SuperFrost®Plus slides. All the retinal sections evaluated by histochemistry were selected at a depth of 400–600 μm from the ON. Approximately 24 consecutive slides were prepared for each retina; each slide contained six tissue sections. For each ON, 16 consecutive slides were prepared, each slide contained eight tissue sections. Immunohistochemistry was performed as previously described (Lechauve et al., 2014; Cwerman-Thibault et al., 2017). To clarify the subcellular distribution of neuroglobin and apoptosis inducing factor, 5 retinas from control mice, both retinas for 5 *Ngb*-treated *Hq* and both retinas for 5 *Aifm1*-treated *Hq* were processed. To obtain retinas flattened into whole mounts with the vitreal side uppermost (corresponding to the GCL and

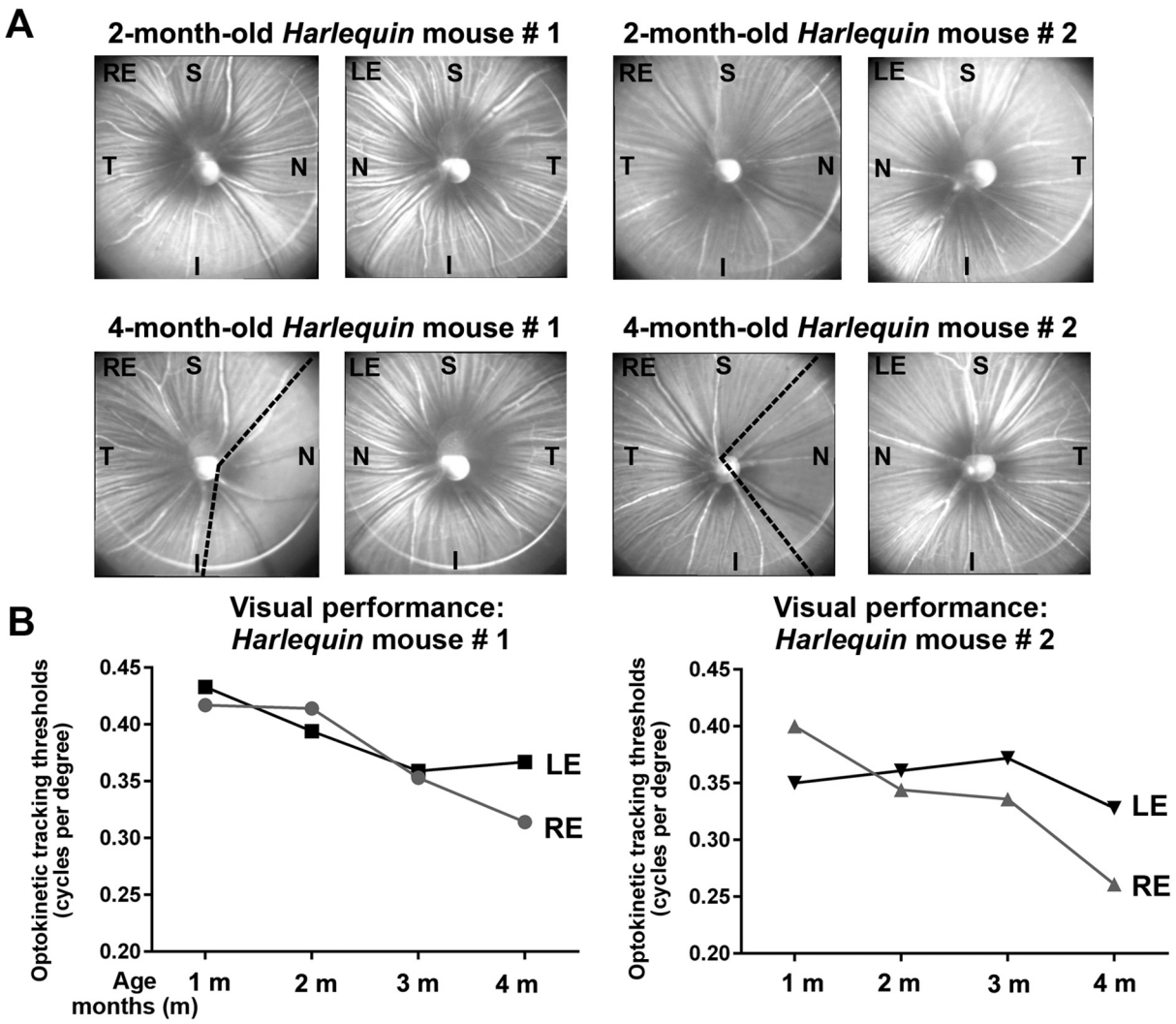

Fig. 1. Morphologic and functional evaluation of eyes from *Harlequin* mice before gene therapy.
Harlequin mice were evaluated monthly from 1 to 4 months of age with: (a) a confocal scanning laser ophthalmoscope to obtain *in vivo* fundus imaging and compare each region of the retinas and (b) the OptoMotry system to estimate the visual function by recording the optomotor tracking responses for the right and left eyes separately.
A. Fundus images of right eyes (RE) and left eyes (LE) from two *Hq* mice aged 2 and 4 months are shown. In each *en face* SLO image, different regions of the retina are illustrated: nasal (N), temporal (T), superior (S), and inferior (I). The fiber loss in the nasal area of the right eyes of *Hq* mice at 4 months is illustrated by the broken black lines.
B. The OptoMotry© set-up enabled to determine the spatial sensitivity of mice using the optomotor tracking responses (cycles per degree) for the left and right eyes, independently scored (clockwise and counterclockwise responses, respectively) under photopic conditions at 100% contrast. The two mice showed in A were evaluated monthly between the age of 1 and 4 months. Right and left eye sensitivities are illustrated for each mouse (left and right panels).

the RNFL), eyes were enucleated and their anterior segment and choroid were removed in order to treat each retina with 4% PFA at 4 °C overnight. Next day, the retinas were washed twice with PBS (15 min/wash) then permeabilized with PBS and 1% Triton X-100 for 10 min. They were then incubated in the blocking buffer for 2 h at room temperature with gentle stirring. Primary antibodies were added to the blocking buffer at the appropriate concentrations (Table 2), and the retinas were incubated overnight at 4 °C with gentle stirring. Next day, the retinas were washed twice with PBS (15 min/wash) at room temperature and incubated with secondary antibodies and DAPI for 2–3 h at room temperature in the dark with gentle stirring. After this incubation, the retinas were rinsed twice with PBS (15 min/wash), and four incisions were made at intervals around the tissue under binocular magnification. The retinas were then carefully flattened and mounted on glass slides with the vitreal side uppermost. The concentrations of the primary and secondary antibodies used for immunohistochemistry are shown in Table 2.

2.7. *In situ proximity ligation assay*

To establish whether the neuroglobin could interact with Aif in mouse retinas we used the Duolink Kit (Sigma-Aldrich, St. Louis, MO), which is based on *in situ* proximity ligation assay (PLA) technology. This technology allows visualization of protein interactions in fixed tissues or cultured cells (Hegazy et al., 2020). In the assay, oligonucleotide-tagged secondary antibodies are linked with circle-forming oligonucleotides. If two antigens, detected by primary antibodies derived from different species, are in close proximity (<40 nm) to each other, after the ligation step of the two linker oligonucleotides, the rolling circle amplification using complementary fluorophore-tagged oligonucleotide probes results in fluorescent puncta at the interaction site. The detection was performed with the Red detection Reagents (emission at 594 nm and excitation at 624 nm).

The PLA technology was efficient to demonstrate protein interactions in rodent retinal sections (Cwerman-Thibault et al., 2015;

Table 1
Characteristics of mice enrolled in the experiments of gene therapy.

	Injection with AAV2/2-*Ngb*		Injection with AAV2/2-*Aifm1*	
Number of treated *Harlequin* mice	28		24	
Mouse ages when the treatment was performed (weeks) as mean ± S.E.M	16.74 ± 0.53		15.76 ± 0.62	
Treated eye	Right = 14	Left = 14	Right = 11	Left = 13
Mean Optomotry performance of each eye before injection (T = 0 m)	0.368 (RE)	0.327 (LE)	0.3770 (RE)	0.3074 (LE)
P treated *vs* untreated: T = 0 m Wilcoxon signed rank test	0.0011 (**)		0.0011 (**)	
Mean Optomotry performance of each eye 6 months post-injection (T ~ 6 m)	Untreated eye: 0.128	Treated eye: 0.246	Untreated eye: 0.1503	Treated eye: 0.2564
P treated *vs* untreated (T ~ 6 m) Wilcoxon signed rank test	<0.0001 (****)		<0.0001 (****)	
Mice lost before the end of the experiment	1 (died ~2 months post-injection)		0	
Mice which developed cataracts impeding the assessment of visual function	2		1	
Total mice evaluated with the OptoMotry devise	25		23	
Time between the injection and the euthanasia (weeks) as mean ± S.E.M	25.26 ± 1.35		25.67 ± 1.79	

Harlequin mice did not have the same age while gene therapy was performed, the eye injected was selected by the evaluation of mice monthly until 4 months of age using the cSLO and the OptoMotry system. Comparison of right and left eyes in terms of visual acuity was performed with the non-parametric Wilcoxon signed-ranks test (GraphPad Prism 8.0 software). Additionally, treatment duration may vary because mice behaved differently with regard to ataxia and their sacrifice for their well-fare may have occurred before the planned 6 months. The means for mouse age while gene therapy was performed and the duration of the experiment for the 51 animals were expressed in weeks.

Noble et al., 2016; Sakagami et al., 2017). Assays were performed with retinal sections from 4 control mice aged 8–10 months according to the manufacturer's instructions. The following combination of primary antibodies were used: (a) mouse monoclonal antibody against Ndufb6 (complex I subunit) + rabbit polyclonal antibody against Nd6 (complex I subunit); this combination is expected to generate positive PLA signals; (b) mouse monoclonal antibody against Ngb + rabbit polyclonal antibody against Nd6 (complex I subunit); (c) mouse monoclonal antibody against Ndufb6 (complex I subunit) + rabbit polyclonal antibody against Aif; (d) mouse monoclonal antibody against Vdac (Voltage-dependent anion channel of the outer mitochondrial membrane) + rabbit polyclonal antibody against Ngb; this combination of primary antibodies should lead to positive PLA signals since Ngb and Vdac proteins have been described as physically interacting (Yu et al., 2013b); (e) mouse monoclonal antibody against Aif + rabbit polyclonal antibody against Ngb; (f) mouse monoclonal antibody against Ngb + rabbit polyclonal antibody against Aif. Briefly, retinal sections were incubated overnight at 4 °C with the primary antibodies; the next day after washing tissue sections were with Duolink PLA probes MINUS and PLUS for 1 h at 37 °C. A Duolink *in situ* detection kit was used for the ligation and amplification steps and DAPI was used to stain the nuclei. The images were captured using a confocal microscope with 40× objective. The red spots indicate the existence of a specific interaction between the proteins

Table 2
Antibody description.

Antibody target or reagent	Type	Assay: concentration	Supplier, catalog no.
BRN3A	Monoclonal	IIF: 8 μg/mL	Chemicon, MAB1585
GFP	Polyclonal	IIF:1.5 μg/mL	Torrey Pines Biolabs, TP401
Neuroglobin, Ngb	Polyclonal	IIF: 5 μg/mL	Sigma-Aldrich, N-7162
Neuroglobin, Ngb	Monoclonal	IIF: 5 μg/mL	Biovedor, Clone 13C8
Neuroglobin, Ngb	Polyclonal	Western: 2 μg/mL	Eurogentec: 2 immunogen peptides against the human protein; amino acids 43–58 and 136–151*#
Neuroglobin, Ngb	Polyclonal	Western: 1 μg/mL	Santa Cruz, Sc-30144
β-actin	Monoclonal	Western: 0.2 μg/mL	Sigma-Aldrich, A5316
Tomm20	Monoclonal	IIF: 5 μg/mL Western: 1.25 μg/mL	Abcam, ab56783
Aif	Polyclonal	IIF: 2.5 μg/mL Western: 0.05 μg/mL	Abcam, ab32516
Aif	Monoclonal	IIF: 2.5 μg/mL Western: 0.05 μg/mL	ThermoFisher Scientific, Clone 4E7E11
Gfap	Polyclonal	IIF: 2.9 μg/mL	Dako, Z0334
Gfap	Monoclonal	IIF: 2 μg/mL	Sigma-Aldrich, G3893
Vdac	Polyclonal	IIF: 5 μg/mL	Ab 15,895
Ndufb6	Monoclonal	IIF: 5 μg/mL	Abcam, Ab 110244, clone 21C11BC11
Nd6	Polyclonal	IIF: 1 μg/mL	Abcam, Ab 81212
ATP synthase subunit β	Monoclonal	IIF: 1 μg/mL	Thermo-Fischer Scientific Ma1-930 (clone 4.3E8.D10)
Ndufa9	Monoclonal	IIF: 1 μg/mL	Thermo-Fischer Scientific (clone 20C11B11B11)
Opa1	Polyclonal	IIF: 1 μg/mL	Abcam, Ab 4236
Cytochrome C	Monoclonal	IIF: 2 μg/mL	Thermo-Fischer Scientific, MA5-11674 (clone 7H8.2C12)
NF200	Polyclonal	IIF: 1 μg/mL	Sigma-Aldrich, N4142
β3-tubulin	Polyclonal	IIF: 1 μg/mL	Abcam, ab18207
Alexa 488	Anti-IgG, rabbit	IIF: 4 μg/mL	Life Technologies, A11008
Alexa 594	Anti-IgG, mouse	IIF: 4 μg/mL	Life Technologies, A11005
Goat anti-rabbit IgG	Goat anti-rabbit IgG, horseradish peroxidase conjugate	Western: 0.05 μg/mL	Jackson ImmunoResearch Laboratories, 111-035-144
Goat anti-mouse IgG	Goat anti-mouse IgG, horseradish peroxidase conjugate	Western: 0.05 μg/mL	Jackson ImmunoResearch Laboratories, 115-035-003
DAPI(4′,6-diamidino-2-phenylindole, dihydrochloride)	Nucleic acid stain	IIF: 2 μg/mL	Life Technologies, D1306

Abbreviations: IIF, indirect immunofluorescence (for retinal or optic-nerve sections).

* The human (Q9NPG2) and mouse (Q9ER97) sequences for the neuroglobin protein have 94% identity (151 amino acids). Concerning the two peptides chosen for raising antibodies in rabbits, they are identical except for amino acid # 46: the cysteine in the human protein is replaced by a glycine in the mouse protein.

This antibody was no more available from Abcam; it can be replaced by the antibody (ab214224).

recognized by the primary antibodies. Negative control assays were performed by combining anti-Aif and Ndufb6 antibodies, anti- or Ngb and Nd6 antibodies; indeed these proteins are not expected to physically bind to each other. Additional technical negative controls were performed omitting one of the two primary antibodies; they will reveal PLA probe background in mouse retinal sections. Confocal microscope visualizations were accomplished by three independent researchers blinded for the experiments; antibodies used were summarized in Table 2. Five independent control mice aged between 8 and 10 months were subjected to the PLA assay.

2.8. Confocal microscopy and image analyses

Fluorescent labeling was visualized with a confocal laser scanning microscope (Olympus FV1000 or Leica TCS SP8). Images were acquired with Olympus FluoView® or LAS X software. The images were taken with the 40× objective and the 60× objective applying a zoom factor of 2.5 which allows the visualization of a smaller section with the same resolution. Retinal sections and retinal whole mounts were also scanned at 40× magnification with the digital whole-slide scanner NanoZoomer Digital Pathology 2.0 HT scanner (Hamamatsu Photonics), using the Fluorescence Unit option (L11600–05) and the NanoZoomer's 3-CCD TDI camera.

2.8.1. Cell number count

To count the number of RGCs, the NDP viewer software was used with the reconstructed digital images of retinal sections labeled with the antibody against the nuclear factor Brn3a, which is largely used to estimate the overall RGC population in rodents (Nadal-Nicolas et al., 2012). For each mouse, the entire lengths of the GCL from 3 to 5 retinal sections were manually counted to obtain the total number of: (a) nuclei stained with DAPI; (b) neurons that gave a positive signal with the Brn3a antibody, *i.e.*; RGCs; (c) cells labeled with the GFP antibody; (d) neurons double labeled with GFP and Brn3a antibodies. The digital images used for cell number estimation were obtained for 2–3 independent labeling experiments; additionally cell numbers were obtained by three experimenters who were blinded to the age of mice and the vector administered.

For retinal whole mounts, sections between 0.15 and 1 mm^2 were selected in the peripheral areas as sampling boxes along quadrant radii at 2 to 3.5 mm distance from the optic nerve head. Within each section, the number of Brn3a-positive cells was manually determined; simultaneously the β3-tubulin labeling was examined and each BRN3A-positive cell was categorized in either one of the following groups: a) neurons exhibiting strong β3-tubulin staining and up to 4 dendritic connections with neurons or their terminals in their vicinity; b) neurons exhibiting weak β3-tubulin staining and few connections with their neighboring neurons. Moreover for each evaluated whole-mounted retina, the entire surface of the reconstructed image was estimated, by outlining each petal of the sample with the freehand drawing tool of the NDP viewer software. Hence, the following data were generated: number of Brn3a-positive cells per mm^2, number of β3-tubulin positive cells per mm^2, percentage of Brn3a-positive cells with either a preserved or deteriorated morphology relative to the total amount of BRN3A-poisitve cells and the surface of the retinas expressed in mm^2 (Table 5).

2.8.2. Fluorescent signal intensity and RGC axon number measurements

ImageJ Fiji-win64 software (http://imagej.nih.gov/ij) was used to determine (a) the intensity of Gfap staining in retinal or ON sections; (b) the fluorescent signal of the β3-tubulin in retinal sections; and (c) the number of fluorescent spots revealed by the NF200 antibody in ON sections.

Reconstructed retinal sections were generated by the NDP 2.0 HT scanner and exported as a tiff image. With the ImageJ software, binary images were created for four sections per mouse and, after thresholding, the Gfap or β3-tubulin signal intensities were estimated by measuring the "mean fluorescence," using the Analyze/Measure tool of the software.

To estimate the IPL thickness, we used reconstructed sections for four retinas per mouse labeled with the anti β3-tubulin antibody. The central region was chosen from each of them to obtain the linear measurements of four segments drawn with the ruler tool between the inferior part of the INL and the GCL for each retina. The sizes were calculated with the NDP viewer software.

The number of RGC axons was inferred from the fluorescent spots visualized in the labeled ON sections with the antibody against NF200. The total number of "particles", *i.e.*, the number of axons in each image, was automatically estimated for each mouse by analyzing three to six independent ON sections, as described earlier (Lechauve et al., 2014; Cwerman-Thibault et al., 2017).

The intensity of Gfap signals was also determined in ON sections labeled with the antibody against Gfap. Images obtained with the Leica TCS SP8 confocal microscope from 3 to 6 independent ON sections per mouse were processed using the ImageJ software, as for retinal sections.

It should be mentioned that acquisition parameters for the confocal microscope and the digital whole-slide scanner with respect to resolution, intensity, and thickness of synthetic focus images were kept as homogeneous as possible between the specimens from control, untreated *Hq*, and treated *Hq* mice.

2.9. RNA extraction and RT-qPCR assay

Total RNAs purified from retinas were subjected to qPCR essentially using the protocol described previously (Lechauve et al., 2014; Cwerman-Thibault et al., 2017). Briefly, oligo-dT and Superscript II Reverse Transcriptase (Life Technologies, France) were used to reverse transcribe 1 μg of RNA per sample. The reactions were performed with 1/100 of the reverse transcription product, a specific couple of primers per gene evaluated (Table 3) and the Power Sybr-green PCR Master Mix (Applied Biosystems, Life Technologies) and run in the ABI 7500 Fast Real-Time PCR system (Applied Biosystems). Each biological sample was subjected to the assay in triplicates per gene. Ct values were obtained with the ABI 7500 software (v.2.0.6). The mitochondrial *Atp6* gene was used as reference to estimate the steady-state levels of *Ngb* and *Aifm1* mRNAs using the comparative ΔΔCt method.

2.10. Isolation of crude mitochondria from retinal tissues

Twenty-four retinas were isolated from 8-month-old wild-type mice and washed in PBS at 4 °C; next they were homogenized in 1 mL of extraction buffer (0.32 M sucrose, 30 mM Tris-HCl; pH 7.6, 5 mM MgAc, 100 mM KCl, 0.1% fatty acid-free BSA, 5 mM β-mercaptoethanol, and 1 mM PMFS) and crude mitochondria were isolated as we have previously performed from rat retinas (Lechauve et al., 2012). Tissue homogenization was performed with 25 strokes with a hand-driven glass-glass Potter-Elvehjem (2 mL). Homogenates were centrifuged for 8 min at 800 *g* at 4 °C to pellet unbroken cells and nuclei. The pellet was resuspended in 0.5 mL of extraction buffer and homogenized with 25 additional strokes since many mitochondria may remain trapped in it. After centrifugation under the same conditions, both supernatants were assembled and centrifuged once again for 8 min at 800 g at 4 °C to eliminate any remaining nuclear or cell contaminants. Ten percent of the supernatant was conserved at −80 °C and correspond to the "homogenate" fraction. The remaining 90% was centrifuged at 12,000 *g* at 4 °C for 30 min to pellet mitochondria. Ten percent of the supernatant was conserved at −80 °C, it represented the "cytosolic" fraction. Three successive washes of the pellet containing the crude mitochondrial fraction were done in 1 mL of the extraction buffer to eliminate membranes, reticulum endoplasmic, lysosomes and peroxisomes. The last wash was made in the extraction buffer devoid of BSA and PMFS. Before the last high-speed centrifugation, protein concentration was measured using the Bradford assay to get independent aliquots of ~120 μg of

Table 3
Primer pairs used in the RT-qPCR assays.

Transcript	Forward, 5′–3′	Reverse, 5′–3′
Ngb	CTCAGGCAAGGGAAGCATAG	CAGTTAGGTTTCCCCCAAAA
Ngb transgene (synthesized from the vector)	AGGCTATGTCACGAGGTTGG	GGGTAACCCTATGCAGTCGT
Atp6	CGTAATTACAGGCTTCCGACA	AGCTGTAAGCCGGACTGCTA
Aifm1	GGGGGCAAAATGGATAATTC	CTGTTTCTCTTCTGGGGACAG
Aifm1 transgene (synthesized from the vector)	CAACATGAAGATCTCAATGAAGTAG	TCGTCGAGGAATTGCTATTATTT

proteins. After the centrifugation, the supernatant was discarded and each pellet of mitochondrial fraction were stored at −80 °C until use.

For mitoplast preparation, aliquots of 30 μg of mitochondrial pellets (in 100 μL of extraction buffer) were subjected to osmotic shock by addition of 900 μL of 3 mM HEPES (pH 7.4) containing 1× of Halt Protease Inhibitor cocktail (ThermoFisher). After incubation on ice for 15 min, the suspension was centrifuged at 10000 *g* for 15 min to yield the mitoplast pellet (Krasnikov et al., 2005). Samples issued from two independent extractions; *i.e.* homogenates, cytosolic fractions, untreated "crude mitochondrial fraction" and mitoplasts were run in SDS-polyacrylamide gels (30 μg of protein per sample). Western blots were performed as previously described (Lechauve et al., 2014). In brief, after the transfer PVDF membranes were stained with Ponceau S dye (Sigma Aldrich) which gave an estimation of the whole protein pattern in the blot. Primary antibodies against Ngb, Aif, Opa1, β subunit of ATP synthase, Ndufa9 (a subunit of Complex I), Tomm20, or β-actin and secondary antibodies were used successively at appropriate concentrations (Table 2). The specific signals were detected and quantified as described in the next section.

2.11. Western blot analysis

Retinal proteins were purified from nine control mice aged between 7 and 10 months, thirteen untreated *Hq* mice, seven *Ngb*-treated *Hq* mice, and six *Aifm1*-treated *Hq* mice. The untreated *Hq* retinas were from the contralateral untreated eyes of *Ngb*-treated or *Aifm1*-treated mice aged between 9 and 10 months at the time of euthanasia. The retinas were homogenized in 50 μL of 20 mM HEPES, 60 mM mannitol (pH 7.2), and 100 μL/mL of protease inhibitor cocktail (Sigma-Aldrich) at 4 °C with a 200-μL hand-driven glass–glass Potter-Elvehjem micro tissue grinder. Large cellular debris was concentrated by centrifugation (1000 ×*g* for 5 min at 4 °C) and discarded. The amount of protein in the supernatants was then determined with the Bradford assay reagent (Sigma-Aldrich). Thirty micrograms of each sample were subjected to Western blot analysis as described previously (Lechauve et al., 2014). Primary antibodies against neuroglobin, Aif, Tomm20, or β-actin proteins and secondary antibodies were used at appropriate concentrations (Table 2). Specific bands were then detected with Clarity ECL Western Blotting Substrates (Bio-Rad). The apparent molecular mass of each protein was estimated by comparing each signal on the blots to the PageRuler Plus Prestained Protein Ladder (Thermo Scientific). Signals from the membranes were visualized with the G:BOX Chemi and PXi imaging systems (Syngene, Cambridge, UK) then analyzed with GeneSys software (Syngene). Relative quantifications for different membranes were acquired by using the Quantity One analysis software (Bio-Rad, Marnes-la-Coquette, France). Protein steady-state levels were expressed as the ratio of each protein signal relative to the β-actin signal. The antibody against neuroglobin often revealed three bands of approximately 21, 19, and 17 kDa; the whole area covering these bands was quantified as a unique neuroglobin signal that was subsequently normalized against the β-actin signal. ReBlot Plus Strong Solution (Millipore, Molsheim, France) was applied to each PVDF membrane, enabling it to be used with three different antibodies consecutively.

2.12. Tissue homogenate preparation and respiratory chain enzymatic assays

Each optic nerve (ON) was homogenized at 4 °C in 200 μL of extraction buffer (250 mM sucrose, 20 mM Tris, 40 mM KCl, 2 mM EGTA, pH 7.2; BSA (fatty acid free) was added just before use to a final concentration of 1 mg/mL). The ON solution was poured into a hand-driven glass–glass Potter–Elvehjem tissue grinder, and the tissue was broken up by 10–12 passages within the pestle of the homogenizer. Next, the homogenates were centrifuged at low speed (1000 ×*g* for 8 min). The collected supernatants were subjected to two cycles of flash-freezing in dry ice, and the samples were stored at −80 °C until use. Respiratory chain enzymatic activities were measured using a Cary® 50 UV–Vis spectrophotometer (Agilent Technologies); the plots were collected using the Cary 50 Remote Diffuse Reflectance Accessory and the Cary WinUV Scan application. All the traces were baseline corrected and run over the range 360–830 nm.

Two spectrophotometric assays were carried out to measure sequentially the activity of respiratory chain complexes I, IV, and V in a single ON (Lechauve et al., 2014); (Cwerman-Thibault et al., 2017). The first assay measured the activity of complex I (CI: NADH decylubiquinone reductase), which is inhibited by rotenone, and that of complex V (CV: ATP hydrolase), which is inhibited by oligomycin (Benit et al., 2006). The experiments performed at 37 °C can be summarized as follow:

2.12.1. Measurement of Complex I activity

The test is performed in triplicates using 50 μL of each optic nerve homogenate and 1.8 μL of NADH. The NADH solution is freshly prepared in water at 40 mM just before the test and discarded at the end of the day. Each reaction cuvette contains: 225 μL of H_2O and 75 μL of Tris HCl (50 mM, pH 8) complemented with BSA (5 mg/mL). The absorbance at 340 nm when the NADH is added must be about 0.9–1. The oxidation of NADH is monitored at 340 nm for 3 to 5 min corresponding to the linear phase of the reaction. Two μL of rotenone (2 mM) are added and the reaction is continued for 2–4 additional minutes to determine the rate of any rotenone-insensitive activity. The rate of rotenone-sensitive NADH oxidation was taken as a measure of complex I activity.

2.12.2. Measurement of Complex V activity

Adding a freshly prepared mixture containing phosphoenolpyruvate (PEP), ATP, MgCl2, lactate dehydrogenase (LDH) + pyruvate kinase (PK), triggers the ATP hydrolase activity of complex V, which can be inhibited by oligomycin as long as the F0 and F1 components of the enzyme remain bound together. The composition of the mixture is: 5 μL of ATP, 50 mM; 5 μL of PEP, 200 mM; 5 μL of MgCl2, 500 mM, 20 μL of PK + LDH. After 1 min, 3 μL of oligomycin (2.5 mM) are added. Under this condition, maximal complex V activity and maximal oligomycin effect are measured after 1 min. Results were next converted into specific activities using the mean of the three values obtained for each sample. CI and CV activities were expressed as nanomoles of oxidized NADH/min/mg protein, using the extinction coefficient $\varepsilon = 6.22\ mM^{-1}\ cm^{-1}$.

In the second assay, the activity of complex IV (CIV: cytochrome *c* oxidase [ferrocytochrome *c*: oxygen oxidoreductase]) was measured by adding a reduced Cytochrome C (CytC) solution of 2 mM in distilled

water. The CytC was reduced by adding a few grains of sodium dithionite; the solution changed colour from brown to orange-pink when the reduction was complete. The protocol can be summarized as follow:

2.12.3. Measurement of Complex IV activity

The test is performed in triplicates using 30 μL of each optic nerve homogenate. Each reaction cuvette contains at the beginning 300 μL of 10 mM KH_2PO_4 (pH 7.2) and BSA (1 mg/mL). Next, 2 μL of reduced CytC is added to the cuvette; the reaction is initiated by adding 30 μL of the homogenate. The absorbance changes are monitored at 550 nm for 2 min. The rate of CytC oxidation is calculated using the extinction coefficient of 27.2 mM^{-1} cm^{-1}. Results were next converted to specific activities using the mean of the three values obtained and the protein concentration estimated by the Bradford method. The activity of complex IV is expressed as nanomoles of oxidized CytC/min/mg protein.

Protein concentration was quantified by the Bradford method, following the supplier's instructions; the measurements were performed in triplicate, using 3 μL of homogenate per sample. The mean values calculated from the triplicates of each assay was used to estimate the specific activities for each complex.

All the chemicals used for the assays were of the highest grade available from Sigma-Aldrich.

Examples of the two spectrophotometric assays are illustrated in Fig. S1 for the successive measurements of rotenone-sensitive Complex I, oligomycin-sensitive ATPase (Complex V) and for Complex IV. The final concentration of each reagent added per cuvette is also indicated.

2.13. Statistical analysis

Statistical analyses were performed with GraphPad Prism version 8.0.0 for Windows, Software (San Diego, California USA, www.graphpad.com). Since we compared more than two unmatched groups, we need to know whether the groups follow a Gaussian (normal) distribution populations before applying a parametric or nonparametric test. Hence, the D'Agostino-Pearson omnibus normality test was performed to establish the normal distribution of groups. In the case of parametric data, one-way ANOVA (analysis of variance) followed by Tukey's *post hoc* test for multiple comparisons was used; this test compares three or more sets of unpaired measurements, assumed to be sampled from a Gaussian distribution. For nonparametric data, Kruskal-Wallis followed by Dunn's multiple comparisons test was performed; indeed the Kruskal-Wallis test does not assume a normal distribution of the groups. For all analyses, the significance level was set at $\alpha = 0.05$.

Table 4 describes the complete statistical analysis applied for each experiment and the corresponding figures. Reports of statistical significance, *P* values, from GraphPad Prism in each figure are as follow.

$P > 0.05$: ns; $P \leq 0.05$: *; $P \leq 0.01$: **; $P \leq 0.001$: ***; $P \leq 0.0001$: ****.

For the OptoMotry test in control mice (Fig. 10A), the comparison of the visual performance in right and left eyes was performed using the paired parametric significance *t*-test.

3. Results

3.1. Treatment of advanced optic neuropathy in Harlequin mice

As a consequence of the almost complete lack of Aif, *Hq* mice progressively lose retinal neurons. The degenerative process in RGC somas and their axons starts at 3 months of age, leading to the disappearance of approximately half of the RGCs over the subsequent 3 months (Bouaita et al., 2012). In parallel, photoreceptor degeneration begins in mice aged 4–5 months, resulting in the disappearance of electroretinogram (ERG) responses by 10 months of age (Klein et al., 2002). The visual impairment is profound in 10-month-old *Hq* mice relative to aged-matched controls (Lechauve et al., 2014).

Gene therapy using recombinant AAV2/2 vectors including the *Ngb* or *Aifm1* open reading frame (ORF) in association with their respective full-length 5′ and 3′ untranslated regions (UTRs) was performed in *Hq* mice aged 4–5 months to establish whether the pathologic process could be stopped or restrained in spite of its advanced stage. To achieve this goal, we subjected *Hq* mice at 1 month of age and monthly thereafter until the age of 4 months to eye fundus imaging and measured their

Table 4
Statistical summary analysis for the experiments involving the treatment of *Harlequin* mice with neuroglobin.

Experiment	Measurement	Gaussian distribution	One-Way Anova and Tukey's Post-hoc test	Kruskal Wallis and Dunn's Post-hoc test	Figure
qPCR	*Ngb* mRNA level	No	No	Yes	2C
qPCR	*Aifm1* mRNA level	No	No	Yes	2E
Western	Aif protein amount	No	No	Yes	3B
Western	Ngb protein amount	No	No	Yes	3C
Histochemistry (retinas)	RGC number estimation	Yes	Yes	No	5B
Histochemistry (retinas)	Gfaplevels	No	No	Yes	5C
Histochemistry (retinas)	β3-Tubulin levels	No	No	Yes	7B
Histochemistry (retinas)	Thickness of the IPL	Yes	Yes	No	7C
Histochemistry (optic nerves)	Axon number estimations	No	No	Yes	8B
Histochemistry (optic nerves)	Gfap levels	No	No	Yes	8B
Biochemistry	Complex V activity	No	No	Yes	8D
Biochemistry	Complex I activity	Yes	Yes	No	8E
Biochemistry	Complex IV activity	Yes	Yes	No	8E
Electrophysiology	b-wave amplitude	No	No	Yes	9C
Electrophysiology	N1-wave amplitude	No	No	Yes	9D
Electrophysiology	P1-wave amplitude	No	No	Yes	9E
OptoMotry	Visual function *Ngb*-treated mice	No	No	Yes	10B
OptoMotry	Visual function *Aifm1*-treated mice	No	No	Yes	10C

All the experiments performed encompass more than two unmatched groups.
Before choosing the test to apply for evaluating the statistical significance the D'Agostino-Pearson omnibus normality test was performed to establish the normal distribution of the groups.
When the data follow a Gaussian distribution the One-way ANOVA and the Tukey's *post hoc* test for multiple comparisons were applied to compare the groups.
When the data do not follow a Gaussian distribution, the Kruskal-Wallis followed by Dunn's multiple comparisons test was performed.
For all analyses, the significance level was set at $\alpha = 0.05$.

visual performance.

High-resolution confocal scanning laser ophthalmoscopy (cSLO) was used to obtain eye fundus imaging. Each area of the retina (nasal, temporal, inferior, and superior) was visualized in *Hq* and control mice. The fiber bundles (packages of RGC axons) composing the retinal nerve fiber layer (RNFL) appeared as white striations converging to the optic nerve head (Paques et al., 2006).

Visual function was assessed by recording optomotor responses to rotating sinusoidal gratings. During the test, changing the rotational direction of the stimulus enabled to measure separately the performances of the left eye (clockwise rotation) and right eye (counter-clockwise rotation) (Douglas et al., 2005).

Fig. 1 illustrates fundus images of two *Hq* mice aged 2 and 4 months, as well as their visual performance at 1, 2, 3 and 4 months of age (Fig. 1B). In these examples, right eyes were chosen for gene therapy because the disappearance of optic fibers was noticeable on the nasal side of their retinas (Fig. 1A) and was accompanied by a more pronounced decrease in their visual performance relative to that of the contralateral eyes (Fig. 1B).

Next, a single injection of one of the vectors was performed in the vitreous body of the eye that presented the most advanced degenerative progression, the other eye remaining untreated. *Ngb* and *Aifm1* transgenes were cloned in the pAAV-*hrGFP* vector (Fig. S2, panel A). To assess the transduction yield of RGCs in *Hq* retinas 6 months after vector administration immunohistochemistry was performed using an antibody against the GFP (green fluorescent protein) and antibody against BRN3A (Fig. S2, panel B). Reconstructions of retinal sections from injected *Hq* eyes clearly showed homogeneous and intense GFP signal in the ganglion cell layer (GCL), as well as a diffuse signal in the inner plexiform layer, IPL (Fig. S2, panel B). The number of RGCs labeled with the antibody against the transcription factor Brn3a was estimated, as well as the number of neurons that were stained with the anti-GFP antibody (*i.e.*, the transduced neurons in the GCL). Overall, it was evaluated eight retinas from eyes treated with the AAV2/2-*Ngb* vector and eight retinas from eyes treated with the AAV2/2-*Aifm1* vector. Next, four sections from each retina were selected to calculate the total number of cell within the GCL (Dapi staining), the total number of cells within this layer labeled with the anti-GFP antibody (transduced cells), the total number of cells within this layer labeled with the anti-Brn3a antibody (RGCs) and the total number of Brn3a-positve cells which were also labeled with the GFP antibody (transduced RGCs). Eyes treated with AAV2/2-*Ngb* or AAV2/2-*Aifm1* possessed, respectively, 73% or 74% positive-cells for both Brn3a and GFP labeling. Moreover, about 30% of GFP-positive cells were not labeled with the Brn3a antibody; they could correspond to displaced amacrine cells. In the literature, the estimates of RGC percentage in the GCL ranges between 40% and 68%, thus, displaced amacrine cells constitute the rest of neurons in the GCL (Pang and Wu, 2011), (Schlamp et al., 2013) which is quite similar that we have found in this study (Fig. S2, panels C and D). Hence, sustained *Ngb* or *Aifm1* gene expression was observed in many RGCs six months after the treatment.

3.2. Transduced retinas accumulated high levels of Ngb and Aifm1 transcripts and the corresponding proteins

Histochemistry in control mice shows that neuroglobin accumulates in the GCL, the inner nuclear layer (INL), the outer plexiform layer (OPL), and the inner segments of the photoreceptors (IS) (Fig. 2A). Aif is abundant in the GCL and the IPL (Fig. 2B); this latter encompasses the reticulated dendrites of RGCs and the neurons of the INL (horizontal, bipolar, and amacrine cells). The distal part of the OPL is labeled with both antibodies but the Aif antibody gave a stronger signal when compared to the neuroglobin antibody (Fig. 2A and B); the OPL encompasses rod spherules and cone pedicles, site of synaptic connections between photoreceptors, bipolar and horizontal cells these connections possess a high density of mitochondria (Johnson Jr et al., 2007). Confocal images of retinal sections from untreated *Hq* retinas stained with antibodies against neuroglobin or Aif showed weak signals. Moreover, the abundance of neuroglobin or Aif in treated *Hq* retinas was increased when the respective vectors were administered. The intense signals observed in the neurons of the GCL, confirms the efficacy of vector transduction (Fig. 2A and B).

Quantitative polymerase chain reaction (qPCR) assays were performed to compare the abundance of *Ngb* or *Aifm1* transcripts in total RNA preparations from retinas treated with AAV2/2-*Ngb* or AAV2/2-*Aifm1*, as compared to that in total RNA preparations from untreated retinas (Fig. 2C and E). Steady-state levels of *Ngb* transcripts were reduced by approximately 40% in untreated *Hq* retinas relative to those found in control retinas (Fig. 2C). In *Ngb*-treated retinas, there was an approximate seven-fold increase in *Ngb* mRNA amounts, as compared to those found in control retinas (Fig. 2C). As expected, the amount of *Aifm1* mRNA level in *Hq* retinas was only 0.065 times that in controls. AAV2/2-*Aifm1* administration led to a significant increase in the steady-state levels of *Aifm1* mRNA, which reached approximately 0.81 times the amount measured in control retinas (Fig. 2E). Moreover, in *Aifm1*-treated retinas, the endogenous expression of *Ngb* was unchanged when compared to the one in untreated *Hq* retinas (Fig. 2D); similarly *Aifm1* mRNA level remained unchanged in *Ngb*-treated retinas relative to that in untreated *Hq* retinas (Fig. 2F).

To complete qPCR data, retinal protein extracts were subjected to Western blot analysis (Fig. 3). We first evaluated retinas from untreated *Hq* and control mice aged approximately 10 months; in *Hq* retinas, the Aif protein signal represented 11% of that measured in aged-matched controls. Neuroglobin steady-state levels in *Hq* retinas were reduced to approximately 62% to those in aged-matched controls. In contrast, the amount of the mitochondrial protein Tomm20 was not statistically different in untreated control and *Hq* retinas (Fig. 3A). Next, we evaluated the abundance of neuroglobin and Aif in retinas of *Hq* mice that received either of the vectors and in retinas from the contralateral untreated eyes. It is noticeable that two bands with apparent molecular mass of 21 and 17 kDa and in some samples a visible 19 kDa signal were detected with the antibody against Ngb (Fig. 3A, third line). This result was also observed in our previous studies with retinas from rats, *Hq* mice and DBA2/J mice (Lechauve et al., 2012; Lechauve et al., 2014; Cwerman-Thibault et al., 2017). Our hypothesis regarding these forms revealed by the antibody is that they may represent post-translational changes such as multiple phosphorylation or binding with the 14–3-3 protein zeta/delta (YWHAZ) (Jayaraman et al., 2011; Van Acker et al., 2019).

Both neuroglobin and Aif levels increased between two- and three-fold in retinas from eyes treated with the corresponding vector, as compared to the levels in retinas from the untreated eyes (Figs. 3B–D). Moreover, no difference was evidenced in the amount of Tomm20 when untreated and treated *Hq* retinas were compared (Fig. 3B–D). Thus, administering AAV2/2-*Ngb* or AAV2/2-*Aifm1* to *Hq* eyes resulted in increased levels of the corresponding transcripts and proteins in the retinas up to 6 months after they underwent gene therapy.

3.3. Subcellular distribution of neuroglobin and apoptosis inducing factor in mouse retinas

The subcellular localization of neuroglobin has been examined both in tissues and cells; us and others showed that at least a part of the protein is found within the mitochondria (Lechauve et al., 2012; Yu et al., 2012b; Yu et al., 2013b; Baez-Jurado et al., 2018). To shed light on the cellular distribution of neuroglobin and Aif both in control and *Hq* retinas, immunohistochemistry was performed in retinal sections with antibodies against two known mitochondrial proteins Vdac (voltage-dependent anion channel of the outer mitochondrial membrane) and Cytochrome C (small hemoprotein of the inner mitochondrial membrane, which transfers electrons between complex III and complex IV). The confocal images obtained from the double labeling with the

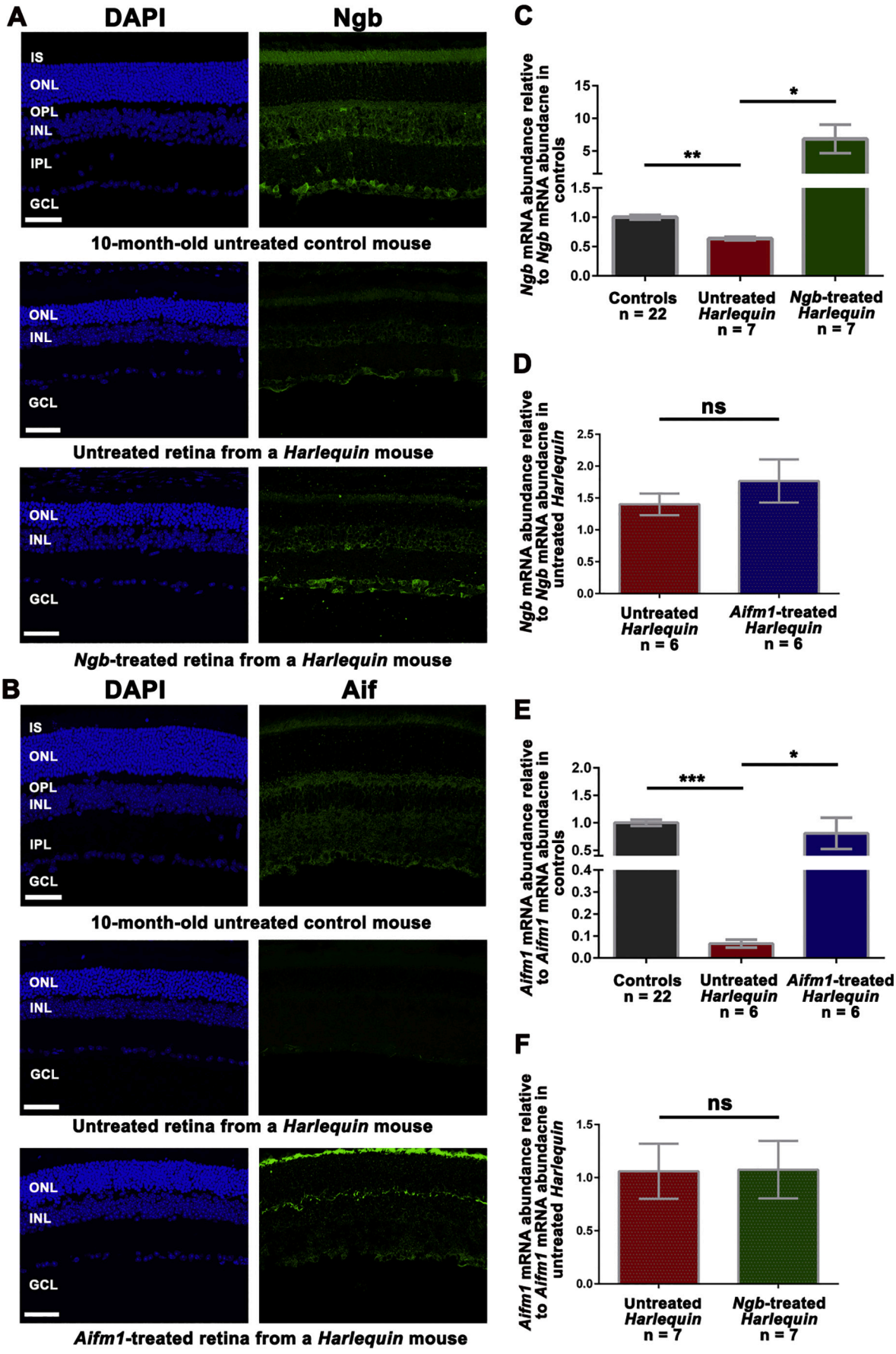

(caption on next page)

Fig. 2. Gene therapy with *Ngb* or *Aifm1* vector results in the accumulation of high levels of the corresponding transcripts and proteins in *Harlequin* Mouse Retinas. (A and B) The abundance and cellular distribution of neuroglobin and Aif proteins were examined by indirect immunofluorescence in retinal sections from two *Hq* mice aged 10 months and treated with each one of the vectors and two untreated aged-matched control mice using specific antibodies against neuroglobin (Ngb) (green, panel A) or Aif (green, panel in B). In control mice both proteins are highly abundant in the GCL, but slight differences were noticed: the Aif signal was more intense than the one of neuroglobin in the IPL, whereas neuroglobin appeared more abundant than Aif in the INL and the IS. Also, the quantities of neuroglobin and Aif were higher in treated *Hq* retinas than in their untreated counterparts, especially in the GCL. Nuclei were stained with DAPI (blue). The concentration used for each antibody is specified in Table 2. The scale bars correspond to 50 μm. Abbreviations: IS, inner segments of photoreceptors; ONL, outer nuclear layer; INL, inner nuclear layer; GCL, ganglion cell layer; OPL, outer plexiform layer; IPL, inner plexiform layer.
(C–F) To estimate the steady-state levels of *Ngb* or *Aifm1* mRNA, RT-qPCR assays were performed using total RNAs from retinas of untreated control mice aged 9–10 months (11 mice) and of *Hq* mice treated with either AAV2/2-*Ngb* (7 mice) or AAV2/2-*Aifm1* (6 mice). For all the mice, both treated and untreated retinas were evaluated. The number of individual retinas evaluated is indicated (n). The steady-state levels of *Ngb* mRNA (panel C) or *Aifm1* mRNA (panel E) found in animals subjected to gene therapy with AAV2/2-*Ngb* or AAV2/2-*Aifm1* respectively, are shown as means ± SEMs after normalization against the mean signals for *Ngb or Aifm1* mRNA measured in retinas from untreated control mice. The steady-state levels of *Ngb* mRNA (panel D) or *Aifm1* mRNA (panel F) found in animals subjected to gene therapy with AAV2/2-*Aifm1* or AAV2/2-*Ngb* respectively, are also illustrated as means ± SEMs after normalization against the mean signals for *Ngb* or *Aifm1* mRNA obtained in retinas from untreated *Hq* mice. The *P* values shown were calculated with respect to data collected from untreated control or *Hq* mice by applying the Kruskal-Wallis test followed by Dunn's multiple comparisons test was performed with the GraphPad Prism 8 software. Specific primers used for *Ngb* and *Aifm1* mRNAs are shown in Table 3. (For interpretation of the references to colour in this figure legend, the reader is referred to the web version of this article.)

antibodies against neuroglobin (Ngb) and Cytochrome C (CytC) allowed to highlight the following observations (Fig. S3): (a) there is a non-negligible degree of colocalization between the two proteins, particularly in the IS, GCL and INL; (b) the signal appeared as fluorescent spots excluded from the nuclei with the two antibodies, evident in the high magnification images, in which cells in the GCL show fluorescent punctuate dots (yellow-orange pixels in the merge panels), suggesting that the proteins localized to the mitochondrial compartment; (c) fluorescent signals for neuroglobin were increased in the GCL of *Hq* retinas treated with the AAV2/2-*Ngb* vector compared to the signal obtained in untreated *Hq* retinas. Besides, the overall cellular distribution of neuroglobin despite its increased abundance in treated retinas did not change.

When the immunolabeling of retinal sections was performed with antibodies against Aif and Vdac (Fig. S4), it was also observed fluorescent signals, as punctuate dots, coinciding in the GCL, IPL and OPL. The slight differences with the neuroglobin signal, evidenced in Fig. 2B, are also observed here such as a stronger signal in the OPL. Equally than for the neuroglobin, the high magnification images in the GCL and IPL illustrate strong intensities of fluorescence, materialized as yellow-orange pixels in the merge panels, indicating that Aif and Vdac localized to the mitochondria in RGCs and their dendrites. Additionally, no changes in the cellular distribution of Aif were evidenced in retinas which received the AAV2/2-*Aifm1* vector (Fig. S4); for instance the nuclei of retinal neurons remained unlabeled.

In an attempt to confirm the presence of both neuroglobin (Ngb) and apoptosis-inducing factor (Aif) in the same mitochondrial compartment classical immunohistochemistry using antibodies against the two proteins was carried out. Fig. 4A illustrates confocal images of retinal sections from a control mouse aged 10 months immunolabeled with antibodies against Ngb and Aif. The immunoreactivity was revealed as punctuate distribution of fluorescent dots excluded from the nuclei which should represent mitochondria and indicated some extent of colocalization between the two proteins. This was noticeable in the high magnification image (Fig. 4A, bottom panel): both the cytoplasm of cells within the GCL and neuronal branching / dendrites within the IPL exhibited yellow-orange pixels which could correspond to regions where both proteins are in close proximity.

Next, to strengthen the postulate that neuroglobin localizes to mitochondria and could be physically associated with different well-known mitochondrial proteins and especially Aif, two type of experiments were performed: (a) *in situ* Proximity Ligation Assay (PLA) using retinal sections; this method allows to visualize, in fixed tissues, a specific interaction between two endogenous proteins if indeed they localize within a <40 nm space (Hegazy et al., 2020); (b) Western blot assays with isolated crude mitochondria and mitoplast fractions which are devoid of the outer membrane and the inner membrane space.

For the assay, antibodies against Ngb, Aif and the following mitochondrial proteins were used: Ndufs1, Nd6 and Ndufb6, three subunits of the respiratory chain complex I (inner mitochondrial membrane and matrix); the voltage-dependent anion channel, Vdac (outer mitochondrial membrane); Opa1, a dynamin-related GTPase involved in mitochondrial dynamics (Del Dotto et al., 2018) and the β subunit of the ATP synthase (Complex V). Negative controls were performed by incubating retinal sections with only one of the primary antibodies, no staining was evidenced in any of the retinal layers (Fig. S5). In the left panel of Fig. 4B are illustrated the results for the following combination of antibodies: anti-Ngb and anti-Ndufb6, anti-Ngb and anti-Opa1, anti-Ngb and anti-Ndufs1, anti-Nd6 and anti-Aif, anti-Ndufs1 and anti-ATP synthase subunit β, anti-Vdac and anti-Ndufb6. Since red spots are absent or very scarce, it can be suggested that the proteins assessed are not located proximal to each other. In contrast, the right panel of Fig. 4B shows numerous bright red dots in almost all the retinal layers, especially the GCL, the IPL, the OPL and the IS for the pair of proteins Nd6 and Ndufb6 as we have previously observed in rat retinal sections (Cwerman-Thibault et al., 2015). Nd6 and Ndufb6 reside in the hydrophobic arm of Complex I (Formosa et al., 2018). Abundant fluorescent spots were also detected when the assay was performed with anti-Opa1 and anti-Aif antibodies, confirming that these two proteins are located in close proximity in retinas as reported in human fibroblasts in which OPA1 was shown to be physically associated with AIF (Zanna et al., 2008). Importantly, numerous bright red dots suggestive of closely apposed binding of the antibodies were observed when the anti-Ngb antibody was combined with anti-Aif, anti-CytC, anti-Vdac, or anti-β subunit of ATP synthase antibody; fluorescent signals were apparent in all the cellular layers (Fig. 4B, right panel). The abundant fluorescent spots evidenced in the PLA assays for these combinations of antibodies indicate that Ngb and the four mitochondrial proteins assessed are located in a proximal environment within the mitochondria. In primary cortical neuronal cultures from mice the interactions between Ngb and CytC or Vdac have been demonstrated (Yu et al., 2012a; Yu et al., 2013b). Additionally, recent publication demonstrated that in the human neuroglobin, five negatively charged residues in their surface are involved in the interaction with CytC complex and allowed electrons transfer between the two proteins (Tejero, 2020). Besides, our results validate the close localization of Ngb with the subunit β of the ATP synthase or this of Ngb with Aif which were demonstrated, by protein interactomics using recombinant mouse Ngb and HN33 cells (fusion of primary hippocampal neurons and the N18TG2 neuroblastoma cell line) under hypoxic conditions (Haines et al., 2012).

Therefore, the PLA assay corroborated the proximity between Ngb and Aif, since numerous bright red dots in the GCL, the IPL and OPL were observed (Fig. 4B and Fig. S5). The IPL and OPL encompass dendrites and axons of RGCs, bipolar cells and photoreceptors (Fig. 4B and Fig. S5); these layers were also strongly stained in the immunohistochemistry assays when both antibodies were used either alone or in

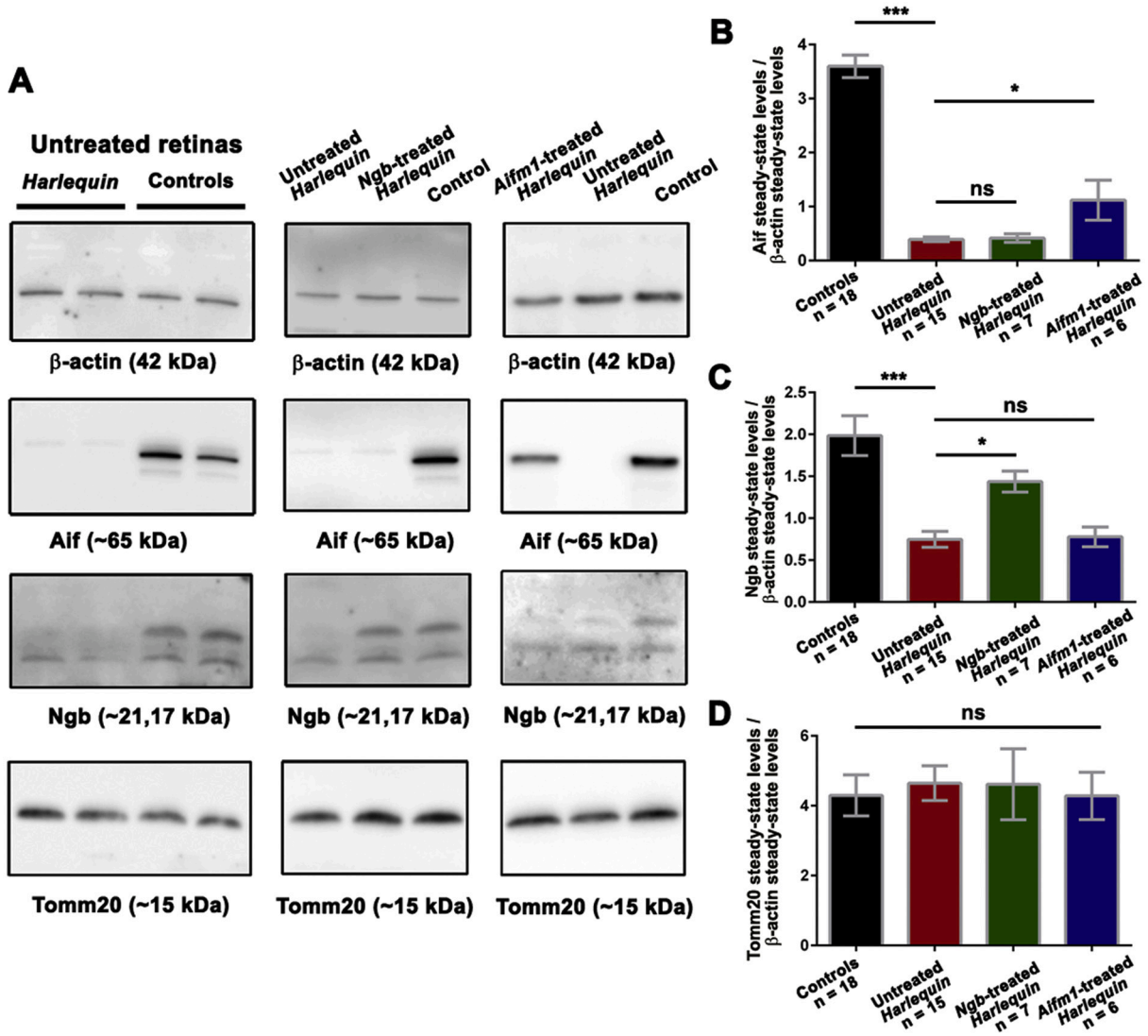

Fig. 3. Relative Amounts of Neuroglobin, Aif, and Tomm20 proteins in Retinas of *Harlequin* and Control Mice.
(A) Representative images obtained when whole-protein extracts (30 μg) from *Hq* and control retinas were subjected to Western blot analysis. The membranes were successively incubated with antibodies against neuroglobin, Aif, Tomm20, and β-actin (as the loading control). The left panel shows two pairs of retinas isolated from untreated *Hq* mice and untreated control mice aged 10 months. Proteins in both retinas of seven *Hq* mice treated with the AAV2/2-*Ngb* vector in one eye and in both retinas of six *Hq* mice treated with the AAV2/2-*Aifm1* vector in one eye were evaluated. The middle and right panels illustrate the results for the two retinas of one *Hq* mouse injected with AAV2/2-*Ngb*, the two retinas of one *Hq* mouse injected with AAV2/2-*Aifm1*, and one retina from an aged-matched control. Specific antibodies against Aif, Tomm20, and β-actin recognized proteins with apparent molecular masses of ~65 kDa, 15 kDa, and ~ 42 kDa, respectively, as was expected from their theoretical molecular mass estimations. The antibody against neuroglobin yielded two main signals, with apparent molecular masses of 21 kDa and 17 kDa.
(B–D) Bar charts showing the relative amounts of Aif, neuroglobin, and Tomm20 mitochondrial proteins in retinas from untreated control eyes and retinas from *Ngb*- or *Aifm1*-treated *Hq* mice in which only one eye was subjected to gene therapy. The number of individual retinas evaluated with the software is indicated (n). There was a two- to three-fold increase in the abundance of neuroglobin and Aif in retinas from the eyes of *Hq* mice treated with the corresponding vectors when compared to the levels in untreated *Hq* retinas. The differences were significant when the results were compared to those obtained in untreated retinas from *Hq* mice ($P = 0.001$ for neuroglobin and $P = 0.014$ for Aif). The *P* values in each group of mice were calculated with respect to data collected as the relative abundance of β-actin in each sample by applying the Kruskal-Wallis test followed by Dunn's multiple comparisons test was performed with the GraphPad Prism 8.

conjunction (Figs. 2, 4A, S3 and S4). The overall PLA responses for Ngb + Aif were comparable to those obtained for Ndufb6 + Nd6, Vdac + Ngb, CytC + Ngb and ATP subunit β + Ngb antibody combinations. Thus, the distance between Ngb and those mitochondrial proteins in mouse retinas might be smaller than 40 nm; indicative that first Ngb localizes to the mitochondria and second that Ngb and Aif are located in a very close environment within the organelle. This vicinity within the organelle could facilitate the functional replacement of one by the other.

Next, enriched mitochondrial fractions obtained by differential centrifugations from adult mouse retinas were subjected to immunoblot analyses. The following samples were examined: homogenates which contain all cellular components (H), crude cytosol having all the subcellular organelles (C), crude mitochondria (M) and mitoplasts (MP) obtained from mitochondrial fractions by osmotic shock resulting in the disruption of the outer mitochondrial membrane; hence, the MP represent vesicles encompassing the inner membrane and matrix compartments of the organelle. Specific antibodies against Ngb, Aif, Opa1, subunit β of the ATP synthase, Ndufa9, Tomm20 and β-actin were successively used to estimate the relative abundance of the corresponding proteins in the compartments assessed (Fig. S6). The antibody against the β-actin was detected in all the fractions as expected. Indeed, it has been described the presence of β-actin in the mitochondrial matrix

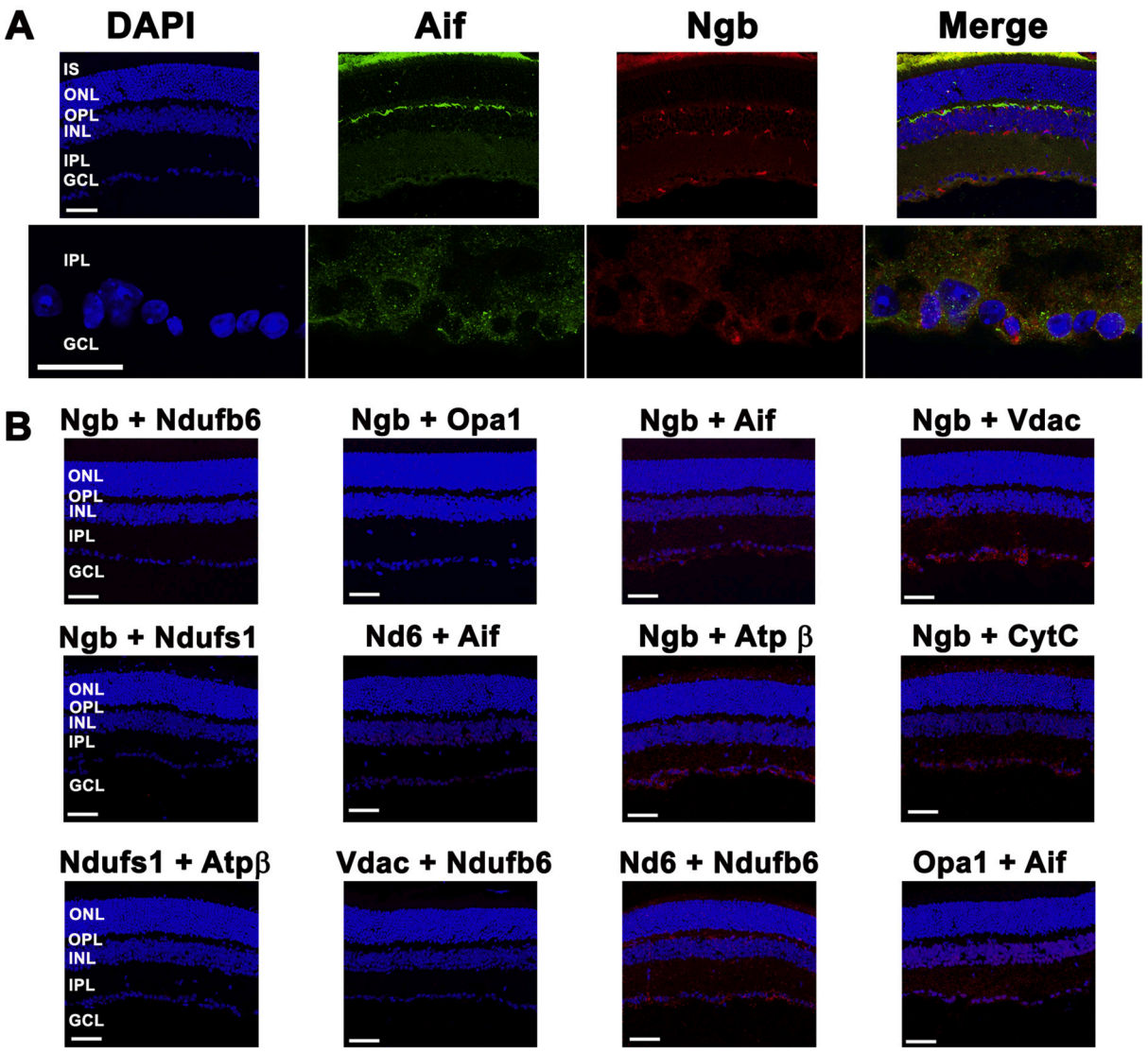

Fig. 4. Subcellular distribution of Neuroglobin and Apoptosis Inducing Factor in mouse retinas.
(A) Immunohistochemistry was performed in control retinas by combining antibodies against neuroglobin (Ngb) and Apoptosis Inducing Factor (Aif). Confocal images obtained are illustrated at two different magnifications: 40× objective (scale bar corresponding to 50 μm in the top panel) and 63× applying a 2.5 zoom (scale bar corresponding to 25 μm). The labeling of the nuclei with DAPI as well as a composite image of the three staining are also shown. In the merge image (rightmost panel), non-negligible extent of overlapping between Ngb and Aif signals is observed in the GCL (especially noticeable in the higher magnification images), and in both the IPL and the IS. Abbreviations: IS, inner segments of photoreceptors; ONL, outer nuclear layer; INL, inner nuclear layer; GCL, ganglion cell layer; OPL, outer plexiform layer; IPL, inner plexiform layer.
(B) Retinal sections were probed with different primary antibodies and subjected to the *in situ* Proximity Ligation Assay (PLA) technology to seek for a direct interaction between neuroglobin (Ngb) and different mitochondrial proteins such as Apoptosis Inducing Factor (Aif). Representative images from confocal visualizations are shown as composites of cell nuclei stained with DAPI and the PLA signals (red dots); the scale bars are equivalent to 50 μm.
Left Panel: Negative results are shown when the following combination of antibodies were used: anti-Ngb (made in rabbit) and anti-Ndufb6 (made in mouse); anti-Ngb (made in rabbit) and anti-Opa1 (made in mouse); anti-Ngb (made in mouse) and anti-Ndufs1 (made in rabbit); anti-Nd6 (made in rabbit) and anti-Aif (made in mouse); anti-Ndufs1 (made in rabbit) and anti-ATP synthase subunit β (made in mouse); anti-Vdac (made in rabbit) and anti-Ndufb6 (made in mouse).
Right Panel: Positive results are recognized by the presence of red dots with the following combination of antibodies: anti-Ngb (made in rabbit) and anti-Aif antibodies (made in mouse); anti-Ngb (made in rabbit) and anti-Vdac (made in mouse); anti-Ngb (made in rabbit) and anti-ATP synthase subunit β (made in mouse); anti-Ngb (made in rabbit) and anti-Cyt-C (made in mouse); anti-Ndufb6 (made in mouse) and anti-Nd6 (made in rabbit); anti-Opa1 (made in rabbit) and anti-Aif (made in mouse). In all the confocal images illustrated, there is an unambiguous occurrence of numerous and intense red fluorescent signals in the GCL, IPL and OPL. Each experiment was performed three times (technical replicates) with four independent control mice aged between 6 and 10 months.
Abbreviations: IS, inner segments of photoreceptors; ONL, outer nuclear layer; INL, inner nuclear layer; GCL, ganglion cell layer; OPL, outer plexiform layer; IPL, inner plexiform layer. (For interpretation of the references to colour in this figure legend, the reader is referred to the web version of this article.)

(Reyes et al., 2011; Xie et al., 2018; Takahashi et al., 2018; Venit et al., 2020). Specific antibodies against Ngb recognized two proteins of ~17 and ~21 kDa apparent molecular masses in homogenates, enriched mitochondrial fractions and mitoplasts. In the contrary, the signal in the cytosol was weak. The overall distribution pattern in each compartment after normalization against the β-actin signal is very similar for all the proteins evaluated. With the exception of Tomm20 which steady-state levels were low in mitoplasts as expected since the protein belongs to the outer mitochondrial membrane disrupted in mitoplasts (Table 7). Therefore, both the 21 and 17 kDa isoforms of Ngb are particularly

enriched in mitochondria, indeed 70 to 79% of the global signal is found in the mitochondrial fraction (Table 7). This result is almost identical to the one estimated for the other mitochondrial proteins assessed, confirming that Ngb does localizes to the mitochondria in mouse retinas.

3.4. Morphologic consequences of gene therapy for retinal cells in Harlequin mice

To establish whether sustained overexpression of *Ngb* or *Aifm1* in *Hq* retinas could have some benefit for neuronal survival, RGC numbers were estimated in retinas from treated and untreated eyes that were subjected to immunostaining for BRN3A. Retinas from *Hq* mice that received either AAV2/2-*Ngb* or AAV2/2-*Aifm1* in one of their eyes (11 mice per vector) were compared to values obtained with age-matched controls. We estimated RGC numbers in untreated control and *Hq* mice aged between 2 and 4 months (young groups) and in untreated control and *Hq* mice aged between 9 and 11 months (old group). For each mouse, the quantity of RGCs within the GCL was determined in four independent retinal sections. Next, the average of these quantities was normalized to the mean obtained for untreated controls aged 2–4

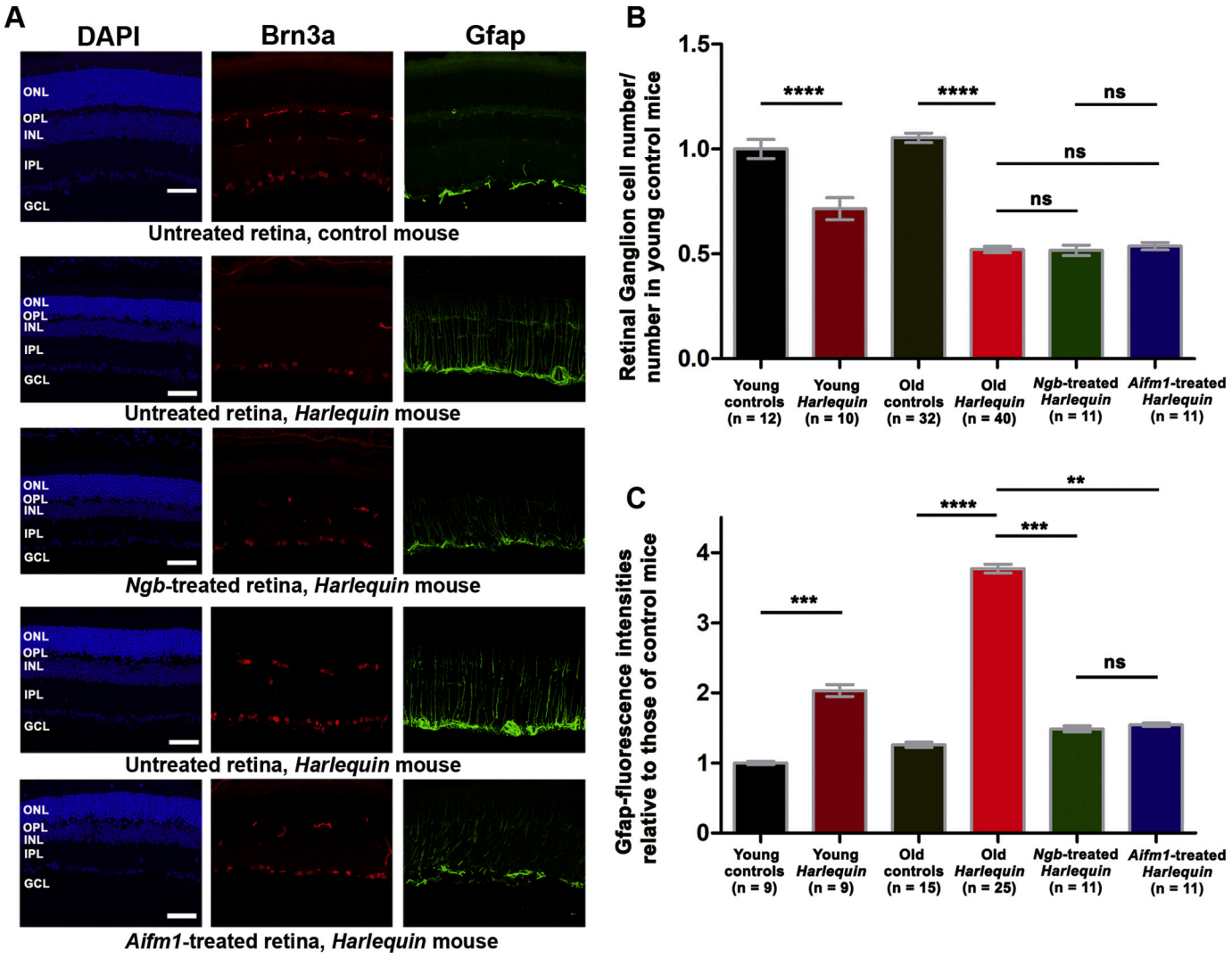

Fig. 5. Characteristics of retinal ganglion cells and Müller glial cells in retinas of *Harlequin* and control mice.
(A) Retinal sections from two *Hq* mice aged ~10 months, in which one eye was subjected to gene therapy with AAV2/2-*Ngb* or AAV2/2-*Aifm1* while the contralateral eye remained untreated, and from one untreated control mouse aged 9 months were subjected to immunohistochemical staining for BRN3A (red) and GFAP (green). Cell nuclei were stained with DAPI (blue) for contrast. BRN3A-positive cells are clearly less numerous in retinas of *Hq* mice (treated or untreated) than in retinas of controls (central panel). In retinas of untreated *Hq* mice, the GFAP signals were more intense in all layers when compared to those in controls, because the glial Müller cell processes extended into the ONL. Reactivity to the anti-GFAP antibody was less prominent in retinas of treated *Hq* mice than in those of controls, irrespective of which vector was administered. Abbreviations: ONL, outer nuclear layer; INL, inner nuclear layer; GCL, ganglion cell layer; OPL, outer plexiform layer; IPL, inner plexiform layer. The scale bar corresponds to 50 μm.
(B) The overall number of RGCs was estimated in *Hq* mouse retinas from animals in which one eye was injected with AAV2/2-*Ngb* (10 mice) or AAV2/2-*Aif*m1 (10 mice) and in retinas from untreated aged-matched controls (19 mice). BRN3A-positive cells in the GCL were counted after reconstructing retinal sections, as described in the Methods section. The bar chart shows the number of RGCs as the mean ± SEM. The number of retinas assessed is shown below the bar for control mice and below each group for *Hq* mice.
(C) The intensity of the GFAP labeling in whole retinas of the mice evaluated by immunohistochemistry with the GFAP antibody was estimated with ImageJ. The bar chart illustrates the data for each mouse group; the number below the bar for control mice and below each group for *Hq* mice corresponds to the number of independent retinas assessed. The *P* values in (B) were calculated by applying one-way ANOVA followed by Tukey's *post hoc* test for multiple comparisons and in (C) were calculated by performing Kruskal-Wallis followed by Dunn's multiple comparisons test was performed. For the two data sets statistics were calculated with the GraphPad Prism 8 software. (For interpretation of the references to colour in this figure legend, the reader is referred to the web version of this article.)

months for all the animals evaluated (Fig. 5B). In the group of young *Hq* mice, a significant diminution of about 30% in the overall number of RGCs relative to young control mice was noticed, $P = 0.001$ (Fig. 5B). The number of RGCs in retinas from treated *Hq* mice, independently of the vector administered, was reduced about 2-fold relative to retinas from control mice and it was not significant different with the one observed in untreated *Hq* mice (Fig. 5B). Consequently, the extent of RGC loss was unchanged six months after vector administration (Fig. 5A and B), indicating that gene therapy in 4–5-month-old *Hq* mice did not protect RGC against degeneration. Progressive optic neuropathy in *Hq* mice is accompanied by glial cell activation (Bouaita et al., 2012; Lechauve et al., 2014). To determine whether AAV2/2-*Ngb* or AAV2/2-*Aifm1* could prevent the active growth of Müller cell processes despite being administered when the disease was at an advanced stage, retinal sections from treated and untreated eyes were immunolabeled with an antibody against glial fibrillary acidic protein (Gfap), a recognized indicator of astrocytes and Müller glial cell activation due to tissue damage (Hippert et al., 2015; Wang et al., 2017). In retinas from control mice, Gfap labeling was limited to the end-feet of Müller cells. In untreated retinas from *Hq* mice, intense Gfap staining extending to the outer nuclear layer (ONL) was evident, indicating hypertrophy of the terminal processes of Müller glial cells in the GCL (Fig. 5A and C). Conversely, there was less Gfap signal in treated *Hq* retinas than in untreated ones, regardless of which vector was injected. The appearance of the labeling was comparable to that observed in control mice, as Gfap signals were observed in the end-feet of Müller cells and in their extensions limited to the IPL (Fig. 5A). Gfap intensities in reconstructed retinas were estimated in the following groups: (a) control mice aged 2–4 months (young controls); (b) untreated *Hq* mice aged 2 to 4 months (young *Harlequin*); (c) untreated controls aged 9–11 months (old controls); (d) untreated *Hq* mice aged 9–11 months (old *Harlequin*); (e) retinas from *Ngb*-treated *Harlequin* mice; (f) retinas from *Aifm1*-treated *Harlequin* mice. Untreated *Hq* mice aged between 2 and 4 months, showed a two-fold increase in the immunoreactivity for Gfap relative to retinas from young controls.

The situation aggravated with age since retinas from untreated old *Hq* mice exhibited a 3.77-fold and 2.99-fold increase in Gfap signal compared to young and old control responses respectively. In contrast, treated *Hq* retinas exhibited signal intensities weaker than those

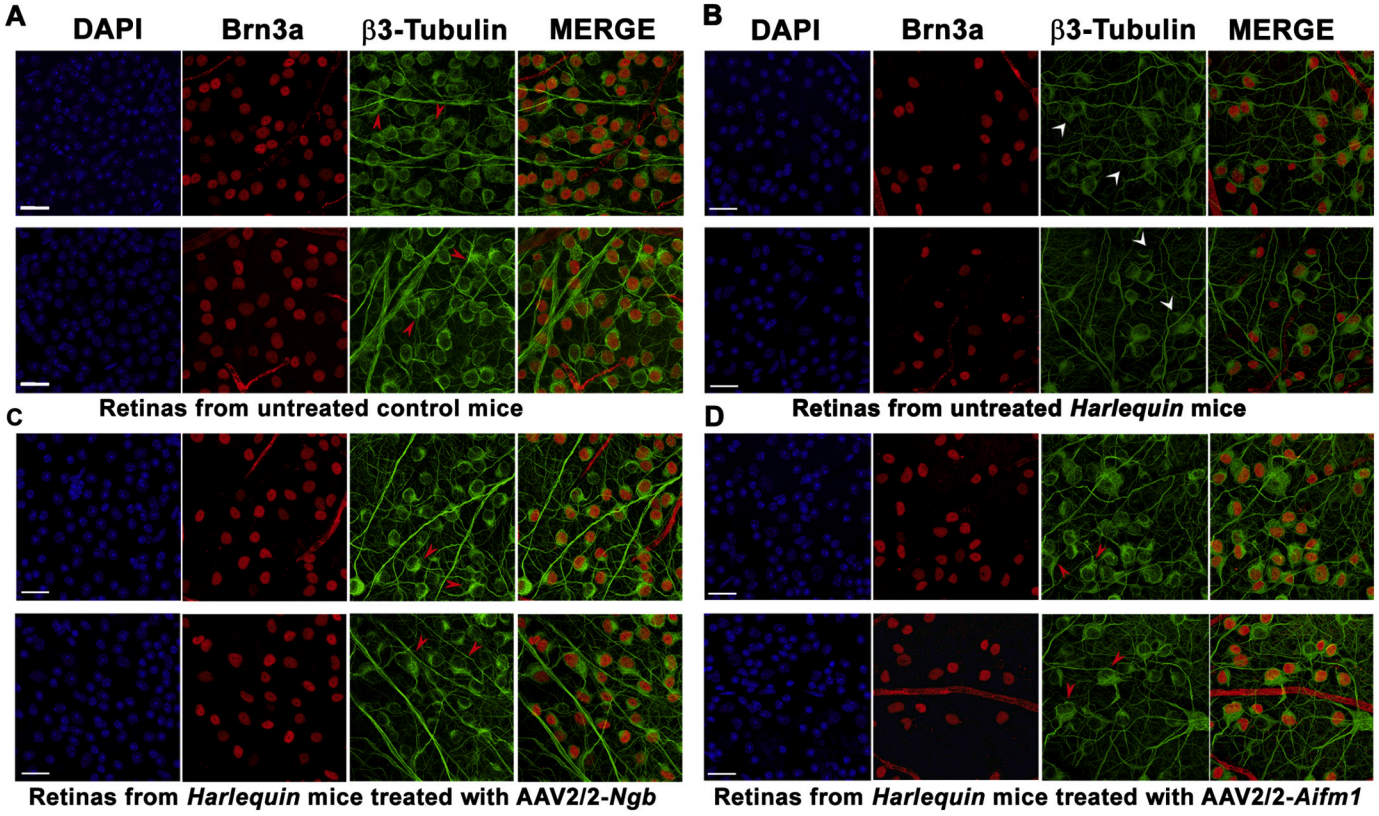

Fig. 6. Morphology of neurons in the ganglion cell layer from control and *Harlequin* mice.

A. Confocal micrographs through the nerve fiber and ganglion cell layers of whole-mount preparations (vitreal side up, with the GCL and NFL visible) of two retinas from 10-month-old untreated control mice. The preparations were subjected to immunohistochemical staining with antibodies against Brn3a (red) and β3-tubulin (green); the nuclei were contrasted with DAPI (blue). A composite image for Brn3a and β3-tubulin labeling is shown in the right panel (MERGE). Retinas from six animals were evaluated, with three or four images being obtained for the central or peripheral regions of each retina. The micrographs illustrate the peripheral region of the retinas. The scale bars correspond to 50 μm. In the β3-tubulin panel (center), two Brn3a-positive cells per panel are highlighted with a red arrowhead. These neurons were chosen because they possessed long dendrites or an extended axon.

B. Confocal micrographs of whole-mount preparations from two retinas obtained from 10-month-old untreated *Hq* mice, processed as described in A. The scale bars correspond to 50 μm. In the β3-tubulin panel (center), two Brn3a-positive cells per retina are highlighted with a white arrowhead, these neurons were chosen since they displayed short dendrites or their axons were indistinguishable.

C. Confocal micrographs of whole-mounted preparations from two retinas obtained from 10-month-old *Hq* mice which were subjected 6 months earlier to AAV2/2-*Ngb* administration; the images were processed as described for Panel A. The scale bars correspond to 50 μm. In the β3-tubulin panel (center), two Brn3a-positive cells per retina are highlighted with a red arrowhead, this neuron was chosen since they displayed evident and preserved axonal / dendritic terminals.

D. Confocal micrographs of whole-mounted preparations of two retinas from 10-month-old *Hq* mice that were subjected 6 months earlier to AAV2/2-*Aifm1* administration. The images were processed as described for Panel A. The scale bars correspond to 50 μm. In the β3-tubulin panel (center), two Brn3a-positive cells per retina are highlighted with a red arrowhead; these neurons were chosen because they displayed evident and preserved axonal/dendritic terminals. (For interpretation of the references to colour in this figure legend, the reader is referred to the web version of this article.)

estimated in retinas from aged-matched untreated *Hq* mice (Fig. 5C). Hence, *Ngb* or *Aifm1* overexpression reduced gliosis of Müller cells, which, if prolonged, could be detrimental to tissue repair and synaptic remodeling by the remaining neurons (Cuenca et al., 2014).

Next, retinas flattened into whole mounts with the vitreal side (corresponding to the GCL and the RNFL) uppermost were labeled with antibodies against Brn3a and β3-tubulin, a member of the tubulin family that forms the microtubules in neurons. Its presence in rodent retinas enables the labeling of somas, dendrites, and axons of RGCs, bipolar cells, and amacrine cells (Jiang et al., 2015; Dordea et al., 2016). We first evaluated retinas from untreated animals aged between 3 and 5 months (Fig. S4). Neuronal degeneration in *Hq* mice was obvious in animals aged ~5 months; the appearance of neurons in the flattened retinas from the control and *Hq* mice aged 3 months was similar (Fig. S4). Next, retinas from *Ngb*-treated eyes or *Aifm1*-treated eyes were compared with retinas from the untreated contralateral eyes and with retinas from aged-matched controls. Fig. 6A shows confocal images corresponding to the periphery of retinas from two control mice aged 10 months; the immunolabeled somas, axons, and dendrites exhibited similar morphologic appearance between them. In untreated *Hq* retinas, the number of neurons was noticeably diminished relative to that in aged-matched controls (Fig. 6B). Immunolabeling of two retinas from *Hq* mice injected with AAV2/2-*Ngb* and two retinas from *Hq* mice injected with AAV2/2-*Aifm1* also revealed fewer neurons. Nevertheless, it was clear that the residual neurons presented a better preservation of axonal and dendritic structures (Fig. 6C and D). The branching complexity and the dendritic arborizations were quite comparable to those observed in control mice and contrasted with those observed in untreated *Hq* retinas. These observations are highlighted in the β3-tubulin panels of Fig. 6B, in which some neurons in *Hq* untreated retinas (identified by white arrowheads) display short/few dendrites whereas several neurons in control and treated *Hq* retinas (identified by red arrowheads) display long dendrites and axons (Fig. 6A, C, and D). Hence, *Ngb* and *Aifm1* overexpression were equally efficient at preserving the structural organization of the surviving neurons in the GCL of *Hq* mice. Next, we evaluated more precisely retinas flattened into whole mounts from untreated and treated *Hq* mice, in order to get a better estimation of cell density population, the percentage of RGCs exhibiting perturbed morphology and the area of the retinas. Table 5 illustrated the results obtained for Brn3a-positive cells / mm^2, β3-tubulin positive cells / mm^2, the comparison of Brn3a-positive cells with preserved morphology or with deteriorated one and the areas of the retinas (mm^2). Three observations can be emphasized: (a) Six retinas from adult wild-type mice issued from a hybrid genetic background C57BL/6 J and B6CBACa were evaluated by immunohistochemistry. Collected data regarding the densities of Brn3a-positive cells (RGCs in the GCL) and β3-tubulin-positive cells (overall neurons in the GCL) are within the means previously described (Salinas-Navarro et al., 2009; Pang and Wu, 2011; Schlamp et al., 2013). Differences observed (areas / cell numbers), may be related to the strain used or the experimental protocol (labeling retinal sections instead using retrograde fluorescent tracers); (b) The proportion of Brn3a-positive cells / mm^2 in *Hq* retinas subjected or not to gene therapy relative to RGC number in control mice was 0.36, 0.44 and 0.50 respectively for untreated *Hq*, *Ngb*-treated and *Aifm1*-treated retinas in agreement with the estimations obtained by counting transversal retinal sections (Fig. 5B). The Brn3A-positive cell densities were not significant different between untreated and treated retinas from *Hq* mice (*P* value are 0.28 or 0.21 for AAV2/2-*Ngb* and AAV2/2-*Aifm1* respectively); (c) Each Brn3a-positive cell was extensively evaluated to establish whether a strong β3-tubulin staining was present along with up to 4 distinguishable connections with neurons nearby or in the contrary the Brn3a-positive cells had a weak β3-tubulin signal and few connections. Unambiguously, the treatment independently of the vector used led to an increase in the number of Brn3a-positive cells displaying a preserved morphology relative to untreated retinas. The half of Brn3a-positive cells in untreated *Hq* retinas were poorly connected to their neighbors.

Table 5
Main features of neurons in the ganglion cell layer from control and *Harlequin* mice.

	Untreated Controls (*n* = 6)	Untreated *Harlequin* (*n* = 8)	*Ngb*-treated *Harlequin* (*n* = 4)	*Aifm1*-treated *Harlequin* (n = 4)
Retinal area (mm^2)	27.19 ± 0.53	23.16 ± 0.86	25.75 ± 0.87	26.63 ± 0.68
β3-tubulin-positive cells / mm^2	2505.0 ± 220.7	953.10 ± 48.54	998.00 ± 78.63	1081.0 ± 164.3
Brn3a-positive cells / mm^2	1719.0 ± 189.7	612.80 ± 56.77	760.6 ± 74.6	853.8 ± 141.2
Total Brn3a-positive cells / retina	46,739.61 ± 5157.94	14,192.45 ± 1314.79	19,585.45 ± 1920.95	22,736.69 ± 3760.16
Brn3a-positive cells with deteriorated morphology and poor β3-tubulin labeling (%)	4.02 ± 0.27	50.12 ± 0.27	9.85 ± 0.12	10.92 ± 0.36
Total number of BRrn3a-positive cells evaluated	4980	3102	1662	1602

Six retinas from adult-wild type mice along with eight retinas from aged-matched untreated *Hq* mice as well as four retinas from *Ngb*-treated and four retinas from *Aifm1*-treated mice were exhaustively evaluated in regard of RGC signals obtained in retinas flattened into whole mounts incubated with antibodies against Brn3a and β3-tubulin. The following estimations are illustrated: (a) Retinal areas; (b) Proportion of Brn3a-positive cells / mm^2; (c) RGC categorization in regards of β3-tubulin signal which reflect their morphology.

Oppositely, in treated retinas the population of residual RGCs with a strong β3-tubulin signal allowing to visualize dendrites connected to nearby neurons was increased by approximately five times. (See Table 5.)

To substantiate these observations, transverse retinal sections were double labeled with antibodies against β3-tubulin and Brn3a. Fig. 7A clearly shows that the intensity of the β3-tubulin staining between the GCL and the INL was diminished in retinas from untreated *Hq* mice. Conversely, retinas from treated *Hq* mice, regardless of which vector was used, exhibited stronger signals relative to those in untreated *Hq* retinas. Fig. S5 illustrates reconstructions of retinal sections for two control mice, two untreated *Hq* mice, and two *Hq* mice treated with AAV2/2-*Ngb* or with AAV2/2-*Aifm1*. The overall intensity of the β3-tubulin signal in retinas from untreated *Hq* mice was weaker than that in retinas from mice treated with AAV2/2-*Ngb* or AAV2/2-*Aifm1* (Fig. S7). Moreover, the thickness of the IPL between the GCL and INL layers was preserved in retinas from treated *Hq* mice when compared to their untreated counterparts (Fig. S8).

Fluorescent signal intensities, obtained with the anti-β3-tubulin antibody, were estimated in reconstructed scanned images (Fig. 7B). The overall β3-tubulin fluorescence intensity in untreated *Hq* retinas was reduced by approximately 50% relative to that in control mice; in contrast, treatment with AAV2/2-*Ngb* or AAV2/2-*Aifm1* resulted in a significant increase in the signals relative to those in untreated *Hq* retinas. Next, the thickness of the IPL (*i.e.* the distance between the GCL and the INL) was measured in β3-tubulin-labeled retinal sections from control mice, treated *Hq* mice, and untreated *Hq* mice. Changes in the thickness of this layer could reflect modifications of RGC synapses with bipolar and amacrine cells, as well as their dendritic distribution in the IPL (Tian, 2012). Fig. 7C shows the estimation of the IPL thickness in retinas from mice treated with AAV2/2-*Ngb* or AAV2/2-*Aifm1*, their untreated counterparts, and age-matched controls. A consistent reduction in thickness was observed in untreated *Hq* retinas. The mean thickness of the IPL was 53.5 ± 4.8 μm and 53.2 ± 2.8 μm in untreated retinas from mice in which the contralateral retinas were treated with

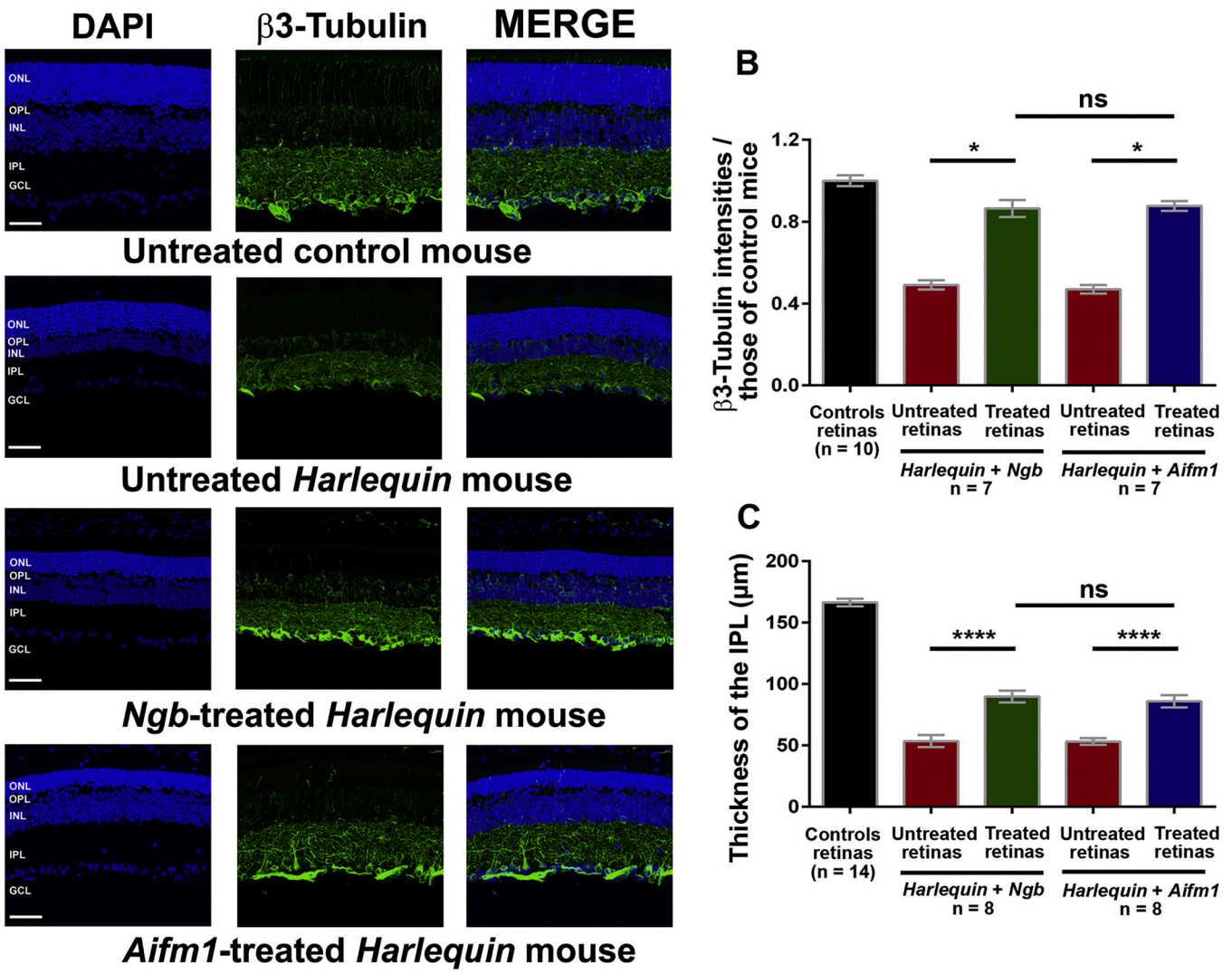

Fig. 7. Characteristics of axonal and dendritic terminals within the inner plexiform layer of retinas from control and *Harlequin* mice.
(A) Confocal images are shown for a retina from a 10-month-old control mouse, a retina from an untreated 10-month-old *Hq* mouse, a retina from the eye of a 10-month-old *Hq* mouse that underwent intravitreal injection of AAV2/2-*Ngb* at 4 months of age, and a retina from the eye of a 10-month-old *Hq* mouse that underwent intravitreal injection of AAV2/2-*Aifm1* at 4 months of age. β3-tubulin labeling (green) and nuclei stained with DAPI (blue) are shown, as well as merged images with both forms of staining (Merge). The scale bars correspond to 50 µm. Abbreviations: ONL, outer nuclear layer; INL, inner nuclear layer; GCL, ganglion cell layer; OPL, outer plexiform layer; IPL, inner plexiform layer.
(B) The bar chart illustrates the normalized values of the fluorescence intensity for β3-tubulin labeling in whole-retina sections reconstructed after scanning with the NDP 2.0 HT scanner; for each mouse, four retinas were evaluated. The values for *Ngb*-treated retinas and *Aifm1*-treated retinas and their untreated counterparts were normalized against the mean fluorescence estimated in 10 retinas from 10-month-old control mice. The number of independent *Hq* mice evaluated with ImageJ is indicated below each bar. Values were plotted using GraphPad Prism 8 as means ± SEMs. The *P* values were determined by applying the Kruskal-Wallis followed by Dunn's multiple comparisons test.
(C) The bar chart illustrates the estimation of the IPL thickness (in µm) by using reconstructed sections for images obtained from retinal sections labeled with the β3-tubulin antibody. Linear measurements of 4 segments drawn between the inferior part of the INL and the GCL in the central area of each retina were calculated with the NDP viewer software. For each mouse, four retinas were evaluated; the number of independent mice evaluated is indicated below each bar of the histogram. Values were plotted as means ± SEMs and the *P* values were determined with the GraphPad Prism 8 software: by applying the one-way ANOVA followed by Tukey's *post hoc* test for multiple comparisons. (For interpretation of the references to colour in this figure legend, the reader is referred to the web version of this article.)

AAV2/2-*Ngb* or AAV2/2-*Aifm1* respectively. The mean thickness of the IPL in retinas from age-matched controls was 166.4 ± 3.1 µm. Administering AAV2/2-*Ngb* or AAV2/2-*Aifm1* to *Hq* retinas significantly prevented IPL reduction, resulting in mean thicknesses of 89.72 ± 4.86 µm and 85.87 ± 4.98 µm, respectively ($P = 0.0078$). Therefore, neuroglobin is as efficient as Aif for protecting, or even refining, the synaptic circuitries of the residual RGCs in *Hq* retinas.

3.5. Optic nerve morphology and function in Harlequin mice subjected to gene therapy

We performed immunohistochemical staining for NF200 in ON cross-sections from treated and untreated eyes of *Hq* mice (Fig. 8A). The number of immunopositive dots in ONs (reflecting the number of RGC axons) from untreated and treated *Hq* eyes was compared to that in ONs from age-matched controls. We observed an approximately two-fold reduction in the number of RGC axons, which correlates with the 50% loss of RGC somas in retinas from *Hq* mice (Fig. 5). There was no

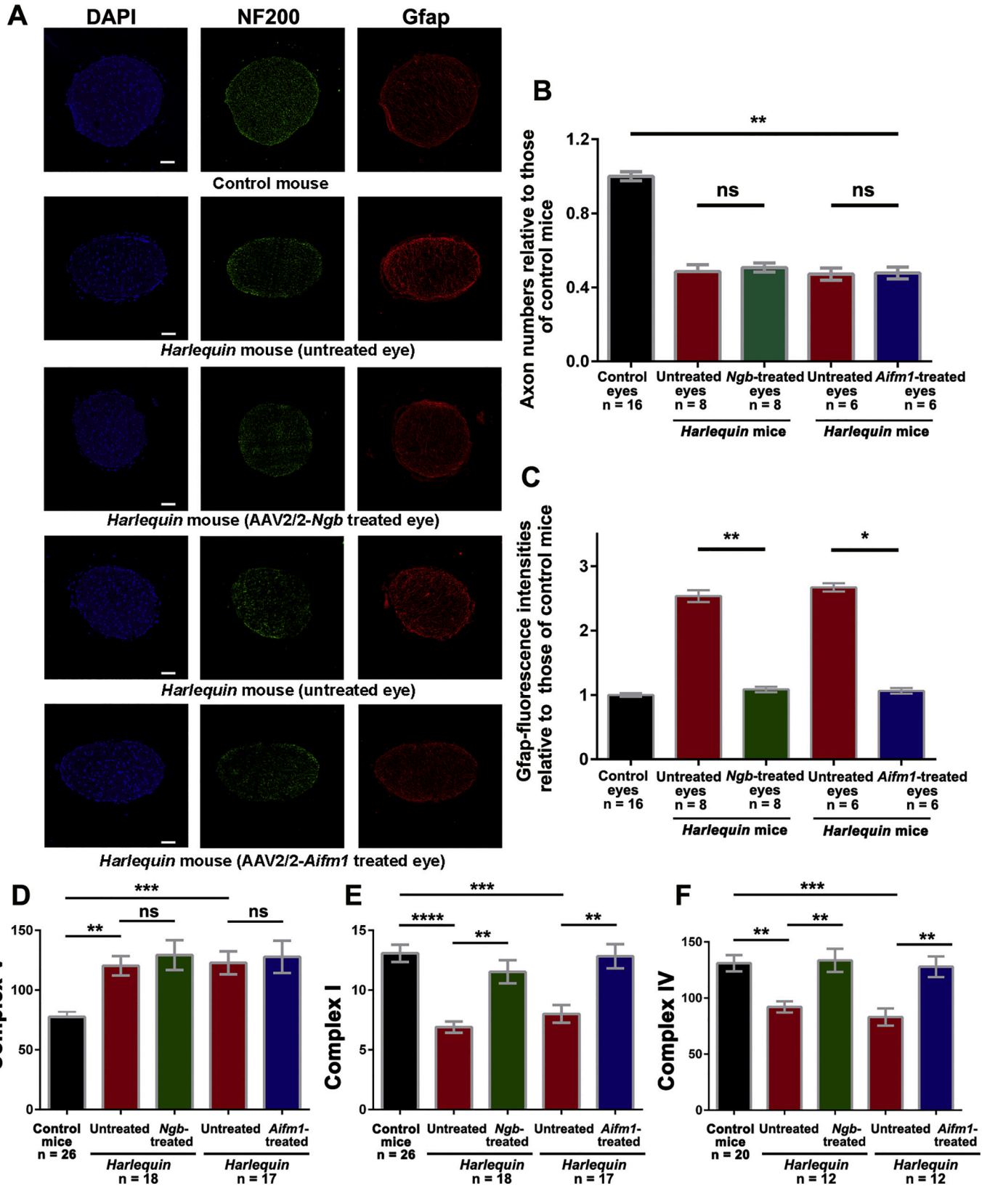

(caption on next page)

Fig. 8. Optic nerve morphology and function in *Harlequin* and control mice.
(A) Proximal ON transverse sections were subjected to immunohistochemical staining with antibodies against NF200 (green) and GFAP (red); the nuclei from astrocytes, microglia, and oligodendrocytes that compose the ON were stained with DAPI (blue). Confocal micrographs from top to bottom correspond to: (a) the ON from an untreated 10-month-old control mouse; (b) the ON from an untreated 10-month-old *Hq* mouse; (c) the contralateral ON from the same mouse as in (b), for which the eye was injected with AAV2/2-*Ngb*; (d) the ON from an untreated 10-month-old *Hq* mouse; (e) the contralateral ON from the same mouse as in (d), for which the eye was injected with AAV2/2-*Aifm1*. The scale bar corresponds to 50 μm.
(B) Bar chart of estimated axon numbers (NF200-positive spots) normalized against the number estimated in 10-month-old control mice. Calculations were made with the ImageJ Fiji-win64 software as the total number of "particles" in each image (three to six images were assessed for each ON) for the following mice: eight untreated control mice aged 10 months; eight *Hq* mice that underwent AAV2/2-*Ngb* injection in one eye; and six *Hq* mice that underwent AAV2/2-*Aifm1* injection in one eye. The treatment and the number of ON sections evaluated per group are specified in the legend below the figure. Values were plotted as means ± SEMs and *P* values were calculated by applying the Kruskal-Wallis followed by Dunn's multiple comparisons test with the GraphPad Prism 8 software.
(C) The mean fluorescence of the GFAP labeling was estimated with the ImageJ Fiji-win64 software. Three to five independent ON sections were examined per mouse for each group. The legends at the bottom indicate the treatment and the number of mice evaluated per group. Normalized values, against the mean fluorescence of 10-month-old control mice, were plotted as means ± SEMs and *P* values were calculated applying the Kruskal-Wallis followed by Dunn's multiple comparisons test with the GraphPad Prism 8 software.
(D to F) The enzymatic activities of complexes I, IV, and V were measured in the following samples from mice aged between 10 and 11 months: (1) ONs from 26 control mice (for complexes I and V) or ONs from 20 control mice (for complex IV); (2) both ONs from 18 mice in which one eye underwent intravitreal injection with AAV2/2-*Ngb* (for complexes I and V) or both ONs from 12 mice in which one eye underwent intravitreal injection with AAV2/2-*Ngb* (for complex IV); and (3) both ONs from 17 mice in which one eye underwent intravitreal injection with AAV2/2-*Aifm1* (for complexes I and V) or both ONs from 12 mice in which one eye underwent intravitreal injection with AAV2/2-*Aifm1* (for complex IV).
The specific enzymatic activities obtained are illustrated in panel D for complex V, panel E for complex I, and panel F for complex IV. The activities of complexes I and V are expressed as nanomoles of oxidized NADH/min/mg protein; the activity of complex IV is expressed as nanomoles of oxidized CytC/min/mg protein. The values shown in each bar chart were plotted as means ± SEMs of triplicates for the specific activities of complex I, complex IV, and complex V. The legend below each bar indicates the treatment and the number of mice evaluated per group. *P* values were calculated with the GraphPad Prism 8 software by applying either the one-way ANOVA followed by Tukey's *post hoc* test for multiple comparisons (Complexes I and IV) or the Kruskal-Wallis followed by Dunn's multiple comparisons test (Complex V). The traces obtained directly from the spectrophotometer for complexes I, V and IV illustrating oxidation-reduction reactions are illustrated in Supplementary Fig. 1. (For interpretation of the references to colour in this figure legend, the reader is referred to the web version of this article.)

significant difference between untreated *Hq* eyes and eyes injected with AAV2/2-*Ngb* or AAV2/2-*Aifm1*. These results confirm that the treatment was performed too late to hinder RGC loss (Fig. 8B).

We also immunolabeled ONs with an antibody against Gfap (Fig. 8A). ONs from treated animals exhibited an evident reduction in Gfap signal intensity, as evidenced in retinal sections (Fig. 5A and C). Fig. 8C shows the mean Gfap fluorescence in ONs from *Ngb*- or *Aifm1*-treated eyes, normalized against the results obtained with ON sections from aged-matched controls. Therefore, the macroglial and astrocyte activation in ONs that accompanies neuronal degeneration in *Hq* retinas was diminished as a result of *Ngb* or *Aifm1* overexpression.

To determine whether gene therapy in *Hq* retinas could lead to an improvement in energy metabolism, we measured the enzymatic activities of respiratory chain complexes I (CI), IV (CIV), and V (CV) by spectrophotometry in ONs from *Hq* mice that underwent AAV2/2-*Ngb* or AAV2/2-*Aifm1* treatment. The CV activity increased by 1.55- to 1.9-fold in all of the ONs isolated from *Hq* mice, as compared to the activity in ONs from control mice (Fig. 8D) as we have previously showed (Lechauve et al., 2014). No significant difference was noticed between ONs from untreated *Hq* eyes and their contralateral counterparts treated with AAV2/2-*Ngb* or AAV2/2-*Aifm1* (Fig. 8D). The specific activity of CI in ONs of untreated *Hq* was diminished by approximately 47% relative to controls (Fig. 8E). The CI activity in mice that received AAV2/2-*Ngb* or AAV2/2-*Aifm1* reached 88% or 98% of the value measured in ONs from control mice. Hence, ONs of *Hq* eyes that received AAV2/2-*Ngb* or AAV2/2-*Aifm1* exhibited, respectively, a 1.67- or 1.6-fold increase in CI activity when compared to the ONs of the contralateral untreated eyes. The values for CI activity measured in the ONs of treated and untreated *Hq* mice were significantly different, irrespective of which vector was administered to the treated animals. Moreover, the CI activity in ONs from treated *Hq* mice was not statistically different from that in control ONs.

Next, we evaluated the enzymatic activity of CIV (cytochrome *c* oxidase) in ONs from the different group of mice (Fig. 8F). When CIV activities of ONs from untreated eyes were compared with values obtained in ONs from control mice, a significant reduction of 30% and 36.6% were observed in *Hq* mice treated in their fellow eyes with AAV2/2-*Ngb* or AAV2/2-*Aifm1* respectively. The activity of CIV in the ONs of eyes treated with AAV2/2-*Ngb* or AAV2/2-*Aifm1* was increased by 45% or 54%, respectively, relative to the activity in their untreated counterparts. Moreover, CIV activity in ONs of eyes subjected to gene therapy, regardless of the vector used, was not statistically different from that in ONs from control mice (Fig. 8F). Thus, *Ngb* or *Aifm1* overexpression efficiently rescued respiratory chain defects in ONs of *Hq* mice, which could have led to an enhancement of the signals that residual RGCs delivered to the visual cortex.

3.6. Overexpression of Ngb and Aifm1 improved visual performance equally in Harlequin mice

To determine whether the preservation of morphologic features of RGCs and the enhanced bioenergetics of the ONs in treated *Hq* mice resulted in a delay on retinal function deterioration, the overall visual performance of the mice was estimated by recording flash visual evoked potentials (F-VEPs) in visual cortices and by measuring the visiomotor behavior of the animals.

F-VEPs, by recording electrical potentials at the visual cortex, give an estimation of the communication integrity over the visual pathway from RGCs through their axons toward the primary visual cortex (Ridder 3rd and Nusinowitz, 2006; Siu and Morley, 2008). Amplitudes and latencies of the recorded reproducible waveforms of positive (P1) and negative (N1) deflections upon light stimulation are calculated. The magnitude of both waves correlates to the number of functional afferent fibers reaching the visual cortex and their synaptic activities (Mead and Tomarev, 2016). In the other hand, latencies reflect nerve influx speed conduction which are impaired by troubles in the myelination process of RGC axons or by severe inflammation of ONs as seen in experimental autoimmune optic neuritis (Matsunaga et al., 2012).

As a complement, *Hq* mice were concomitantly subjected to photopic ERGs to estimate the deterioration of the photoreceptor visual pathway (Tanimoto et al., 2013). Fig. 9A illustrates the plots obtained from one control mouse, one untreated *Hq* mouse aged 9 months and from *Hq* mice injected with AAV2/2-*Ngb* or AAV2/2-*Aifm1*. The amplitudes of b-waves in *Hq* mice, reflecting cone photoreceptor activity, were about 33% of the value measured in age-matched controls (Fig. 9C); no difference was noticed between untreated and treated *Hq* mice. This result is expected since administration of the *Ngb* and *Aifm1* vectors *via* intravitreal injection intend to transduce RGCs, very few vector could

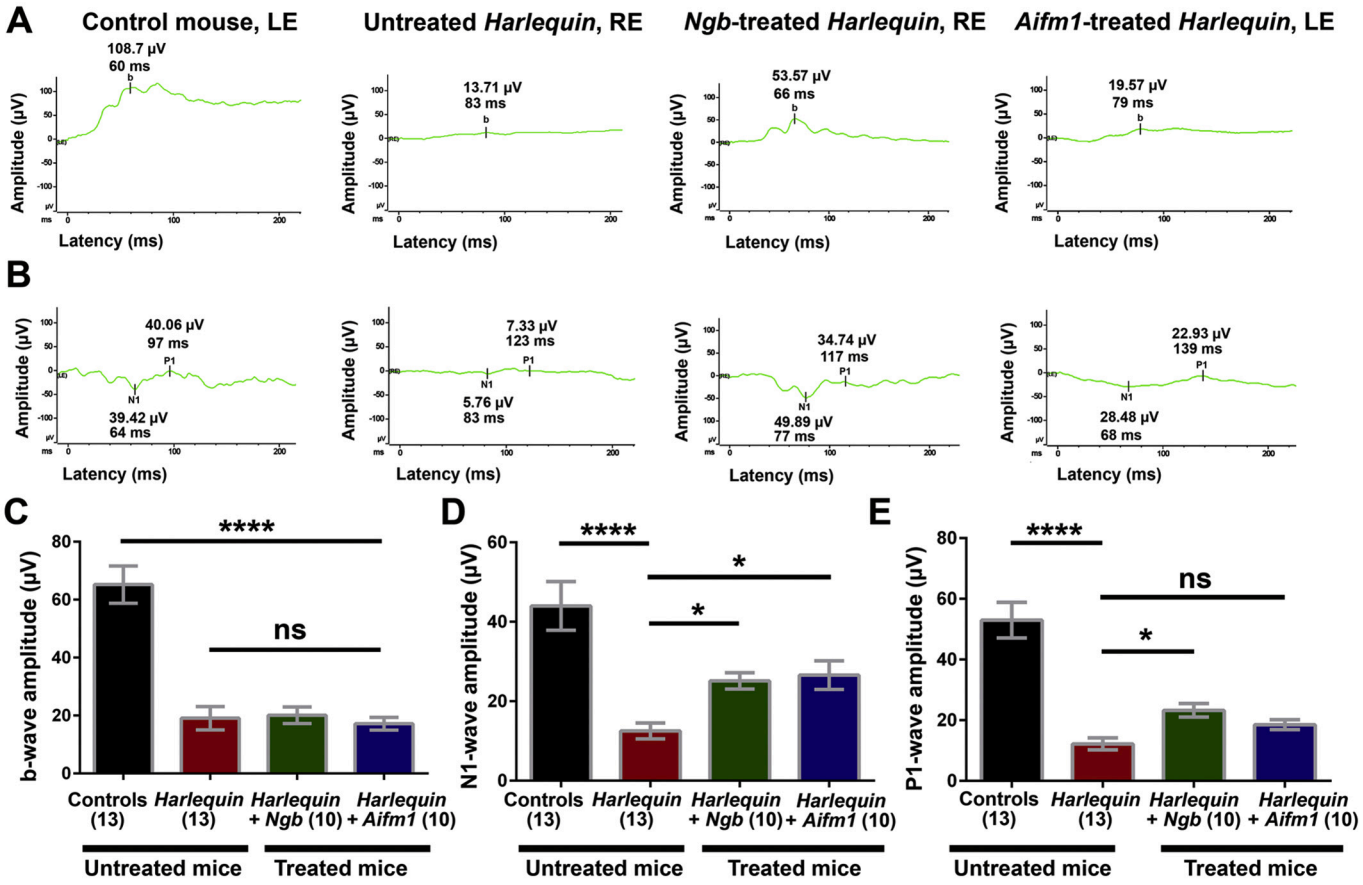

Fig. 9. Electrophysiological hallmarks in control and *Harlequin* mice.

(A) Plots of photopic ERGs recordings. From left to right: the left eye of an untreated 9-month-old control mouse; the right eye of an untreated 9-month-old *Hq* mouse; the right eye of a 10-month-old *Hq* mouse treated with AAV2/2-*Ngb* six months earlier; the left eye of a 10-month-old *Hq* mouse treated with AAV2/2-*Aifm1* six months earlier. At the top of each b-peak are shown the numerical value for its amplitude (expressed in µV) and its latency (expressed in milliseconds, ms).

(B) Plots of F-VEP recordings with the N1 and P1 waveforms from the same animals shown in panel A. At the bottom of each N1 peak and at the top of each P1 peak are shown the numerical values for each amplitude (expressed in µV) and each latency (expressed in milliseconds, ms).

(C) Bar chart of the peak amplitudes of the b-wave for the four groups of mice evaluated: untreated controls, untreated *Hq* mice, *Hq* mice treated with AAV2/2-*Ngb*, and *Hq* mice treated with AAV2/2-*Aifm1*. Values were plotted using GraphPad Prism 8; they correspond to means (left and right eye responses) ± SEMs. *P* values were calculated by performing the Kruskal-Wallis followed by Dunn's multiple comparisons test. The number of animals per group is indicated below each bar chart.

(D) Bar chart of the peak amplitudes of the N1 waves for the four groups of mice evaluated. Values were plotted using GraphPad Prism 8; they correspond to means (left and right eye responses) ± SEMs. *P* values were calculated using the Kruskal-Wallis followed by Dunn's multiple comparisons test. The number of animals per group is indicated below each bar chart.

(E) Bar chart of the peak amplitudes of the P1 waves for the four groups of mice evaluated. Values were plotted using GraphPad Prism 8; they correspond to means (left and right eye responses) ± SEMs. *P* values were calculated by applying the Kruskal-Wallis followed by Dunn's multiple comparisons test. The number of animals per group is indicated below each bar chart.

diffuse up to the outer retina. Besides the serotype 2, we used, does not have an enhanced tropism for photoreceptors (Kay et al., 2013).

Fig. 9B illustrates the traces obtained after F-VEP recording from the same mice. We found no differences in the peak latencies or peak-to-peak amplitudes for N1 and P1 in the tested mice when the responses for right and left cortices were compared. In the mouse optic chiasm, more than 95% of the fibers from the nasal part of the retina decussate and join the uncrossed temporal fibers of the opposite nerve to form the optic tracts (Neveu and Jeffery, 2007). Accordingly, recordings from the right and left visual cortices were not treated separately; indeed, each recording encompassed responses of both transduced and non-transduced RGC axons. The latencies of the N1 and P1 peaks were analogous in all mice evaluated (See Table 6). In contrast, in untreated *Hq* mice aged between 8 and 10 months, there was a statistically significant reduction of approximately 70% in the N1- and P1-wave amplitudes relative to those in controls. AAV2/2-*Ngb* or AAV2/2-*Aifm1* administration in mice aged 4–5 months led to a functional recovery 6 months after treatment (Fig. 9D and E). *Neuroglobin* overexpression resulted in an increase of 200% and 190%, respectively, in the amplitudes of the N1 and P1 waves relative to those of untreated *Hq* mice. Likewise, *Aifm1* overexpression resulted in an increase of 212% and 152% in the amplitudes of the N1 and P1 waves relative to those in aged-matched untreated *Hq* mice. The improvement due to the treatment was not enough to match the responses recorded in control mice of the same age (Fig. 9D and E). Nevertheless, the increased abundance of neuroglobin or Aif in the retinas of *Hq* mice in which the degenerative process has already begun renders residual RGCs capable of providing high electrical inputs to the brain upon light stimulation, resulting in enhanced visual cortex activity.

To determine whether the electrophysiological improvement observed at the cortical level in treated *Hq* mice had physiologic relevance, the spatial visual acuity of treated *Hq* animals was assessed and compared to that of thirteen age-matched controls (Fig. 10A). We observed a significant difference of the head-tracking behavior in untreated eyes of *Hq* mice aged between 10 and 11 months, relative to aged-matched controls; indeed the reduction was of ~70% relative to

Table 6
Electroretinogram and Flash Visual Evoked Potential Components for *Harlequin* and Control mice.

		Untreated control mice (±SEM) [eyes tested = 26]	Untreated *Hq* mice (±SEM) [eyes tested = 26]	*Ngb*-treated mice (±SEM) [eyes tested = 20]	*Aifm1*-treated mice (±SEM) [eyes tested =20]
Photopic ERG	Amplitude of b-wave (μV)	65.21 ± 6.42	19.09 ± 4.05	20.10 ± 2.86	17.18 ± 2.21
	Latency of b-wave (ms)	67.31 ± 2.87	80.46 ± 2.22	82.80 ± 1.88	79.80 ± 2.27
F-PEV	Amplitude of N1-wave (μV)	43.99 ± 6.12	12.53 ± 2.02	25.13 ± 2.07	26.58 ± 3.59
	Latency of N1-wave (ms)	77.27 ± 5.02	72.73 ± 2.95	80.35 ± 3.35	80.50 ± 2.64
	Amplitude of P1-wave (μV)	52.96 ± 5.89	12.20 ± 1.95	23.27 ± 2.25	18.51 ± 1.63
	Latency of P1-wave (ms)	150.70 ± 6.70	127.10 ± 2.92	136.80 ± 3.92	139.70 ± 3.37

The b-wave values correspond to photopic ERG recordings expressed as amplitudes in μV. The data represent the means values ± SEM. There was a significant difference in the b-wave latency in control and *Hq* mice (untreated or treated). The *P* values calculated using the Mann Whitney test were 0.0009, <0.0001 and 0.002 for the following comparisons *vs* control mice: untreated *Hq* mice, *Ngb*-treated *Hq* mice, and *Aif1m*-treated *Hq* mice, respectively. The N1- and P1-waves correspond to F-VEP responses expressed as amplitudes in μV, and the latencies are expressed in milliseconds (ms). The number of individual eyes tested is indicated in brackets below each column header.

Table 7
Proportion of mitochondrial proteins in different subcellular compartments after isolation of crude mitochondria from adult mouse retinas.

Protein	Mitochondrial and Cytosolic signals	Cytosolic/ Total signal	Mitochondrial/ Total signal	Mitoplast/ Mitochondrial signal
Neuroglobin 21 kDa isoform	1.32 ± 0.23	0.31 ± 0.09	0.69 ± 0.09	0.99 ± 0.11
Neuroglobin 17 kDa isoform	1.47 ± 0.28	0.21 ± 0.04	0.79 ± 0.04	1.05 ± 0.06
Apoptosis-Inducing Factor	1.24 ± 0.14	0.13 ± 0.04	0.87 ± 0.047	1.06 ± 0.08
Ndufa9	0.94 ± 0.29	0.13 ± 0.05	0.87 ± 0.05	0.76 ± 0.15
β subunit of ATP synthase	1.42 ± 0.19	0.13 ± 0.03	0.88 ± 0.03	0.84 ± 0.19
Opa1	1.09 ± 0.09	0.09 ± 0.01	0.91 ± 0.01	1.00 ± 0.09
Tomm 20	1.55 ± 0.26	0.08 ± 0.02	0.88 ± 0.03	0.28 ± 0.11

Two independent isolations of "crude" mitochondrial were performed each with both retinas from 12 adult mice. Three series of western blots were carried-out with these biochemical purifications with the following samples: whole homogenates, cytosols, mitochondria, and mitoplasts. The mitoplasts were obtained from osmotic shock of mitochondrial fractions.
Densitometric analyses of each blot were obtained with the Quantity One 1D-analysis software (BioRad); at least six independent measurements were processed from the western blots performed.
The values illustrated are expressed as ratios of each protein signal relative to the β-actin signal; they correspond to the means ± S.E.M.

values measured in control mice ($P < 0.0001$). Moreover, the optomotor tracking abilities of untreated eyes 6 months post-injection of their fellow eyes were 34.8% and 39.9% of the values measured at the beginning of the experiment (Fig. 10B and C, rightmost panels). Conversely, the declines in optomotor responses recorded for treated eyes were significantly less, with responses representing 75.5% and 83.4% of those collected before vector administration for AAV2/2-*Ngb* and AAV2/2-*Aifm1* respectively, *i.e.* a response increased by 2 times relative to the one in their untreated counterparts (Fig. 10B and C, rightmost panels). The evolution of eyes fundus was monitored with cSLO, images for right and left eye of a 4-month-old control mouse are illustrated in Fig. 10A, and both eyes present a homogenous and dense distribution of fiber bundles in the entire retina. Fig. 10B and C (leftmost panel) illustrate images from mice which received AAV2/2-*Ngb* (left eye) or AAV2/2-*Aifm1* (right eye) before vector administration and 6 months later. The untreated eyes before the treatment showed a rather preserved density of fiber bundles, in the contrary the eye selected for gene therapy exhibited RGC axon loss (broken black lines). Six months later, regions depleted in fiber bundles were considerably increased in the four eyes, regardless of the treatment or the vector used. This data is consistent with the estimation of the number of RGCs and their axons (Figs. 5 and 8). The significant improvement of visual function in treated-eyes of *Hq* mice (Fig. 10B and C, rightmost panels) is certainly related to the morphological changes in RGCs within the retina (Figs. 6 and 7), the preservation of the bioenergetics status of their axons (Fig. 8) which conjointly lead to an increase in the visual cortex activity (Fig. 9).

4. Discussion

Inherited optic neuropathies are very often the result of mitochondrial dysfunction in RGCs and their axons, ultimately resulting in neuronal cell death and optic atrophy (Pilz et al., 2017). Two forms of clinical presentation have been identified: (a) an isolated occurrence of visual function loss, of which the most frequents are Leber Hereditary Optic Neuropathy and Autosomal Dominant Optic Atrophy (Carelli et al., 2017); and (b) visual impairment as part of a wider neurologic disorder such as Charcot-Marie-Tooth disease, or Friedreich ataxia (Biousse and Newman, 2017). In both cases, mitochondrial dysfunction is responsible for (1) a profound and irreversible decrease in energy production and (2) amplified oxidative stress that gradually damages proteins, lipids, and nucleic acids. In addition, there is compelling evidence that the disruption of mitochondrial dynamics also leads to optic atrophy because of the resulting disturbances of mitochondrial homeostasis (Ito and Di Polo, 2017). RGCs display peculiar anatomic features that render these neurons particularly vulnerable. Each neuron contributes a long axon, which travels into the RNFL and then toward the optic nerve head. Within the retina, RGC axons are devoid of myelin before they cross the lamina cribrosa (a multilayered network of collagen fibers in the posterior part of sclera through which RGC axons pass as they exit the eye); they become myelinated only after crossing it (Herrera et al., 2019). Obviously, the long, unmyelinated axons require a high density of functional mitochondria for the genesis and conduction of electrical inputs (Yu et al., 2013a). In the posterior part of the ocular globe, more efficient saltatory action potentials take over to propagate visual stimuli to the brain (Carelli et al., 2017).

The absence of Aif in *Hq* mice progressively compromises neuronal survival in their retinas, resulting first in RGC loss and few months later, in photoreceptor degeneration. We and others demonstrated that *Hq* mice aged 10 months or older exhibit severe visual impairment (Klein et al., 2002; Bouaita et al., 2012). We observed that the cone visual pathway, assessed through photopic ERGs (Table 6), was dysfunctional, as the spatial visual acuity in *Hq* mice (Figs. 9 and 10).

The preservation of vision depends on: (a) the electric inputs that are transferred by the photoreceptors to bipolar, amacrine, and horizontal cells (pre-synaptic neurons); (b) the functional connections of RGCs with these pre-synaptic neurons; and (c) the preservation of synaptic

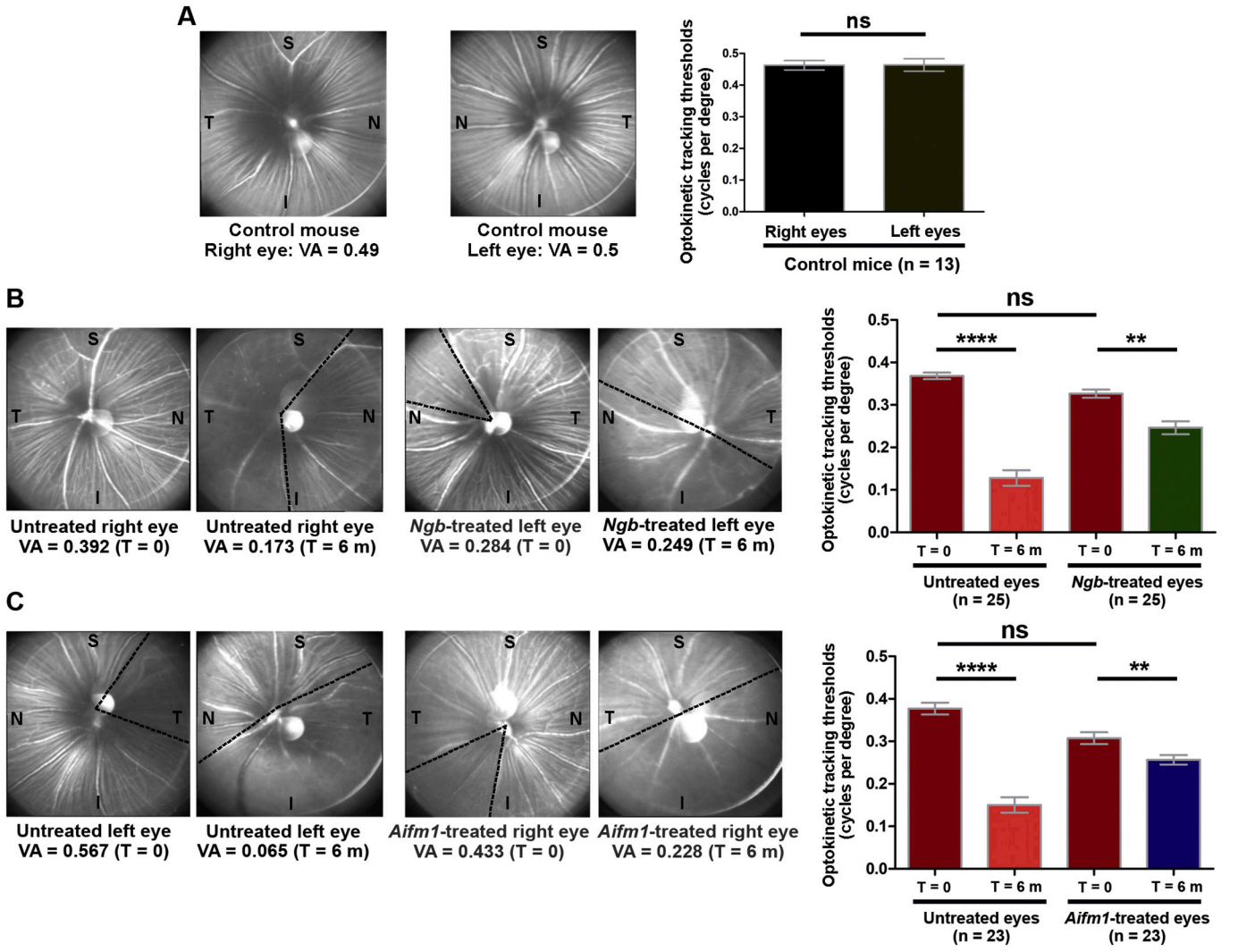

Fig. 10. Spatial visual sensitivity of *Harlequin* mice after gene therapy.

Mice were screened with the OptoMotry system under photopic conditions for measuring optomotor tracking ability (cycles per degree) for left and right eyes, independently scored for clockwise and counterclockwise responses, respectively. These score are considered as an accurate indicator of visual acuity (VA). Eyes fundus images were also illustrated for one control mouse and two *Hq* mice; in each image is annotated the superior (S), inferior (I), nasal (N) and temporal (T) regions of each retina.

(A) Visual acuity (VA) was evaluated with the OptoMotry system in 13 control mice aged between 4 and 11 months. Bar chart illustrates optomotor tracking thresholds for right and lefts eyes expressed in cycles per degree. Values were plotted using GraphPad Prism 8; they correspond to means ± SEMs. The comparison of right and left eyes was performed using the paired parametric significance *t*-test; the *P* value calculated was 0.96 (ns). In the left panel eye fundus for both eyes of one control mouse aged 4 months is shown.

(B–C) The impact of the treatment was sought by subjecting *Hq* mice to the test before vector administration and at 6 months post-injection. The optomotor tracking thresholds expressed in cycles per degree are shown as means ± SEMs of 3 independent measurements obtained 2 days apart for each mouse tested. Evaluations were made at two time points: before treatment ($T = 0$) and 6 months later ($T = 6$ m), immediately before euthanasia. The number of animals per group is indicated below each bar chart. Results for 25 mice treated with AAV2/2-*Ngb* are shown in panel B and results for 23 mice treated with AAV2/2-*Aifm1* are shown in panel C. *P* values were calculated using the GraphPad Prism 8 software by performing the Kruskal-Wallis followed by Dunn's multiple comparisons test.

In the left part of panel B eyes fundus images for both eyes obtained before gene therapy and six months later are shown for one mouse treated with AAV2/2-*Ngb* in its left eye at the age of 4 months and a half; fiber bundle loss is illustrated by the broken black lines.

In the left part of panel C eyes fundus images for both eyes obtained before gene therapy and six months later are shown for one mouse treated with AAV2/2-*Aifm1* in its right eye at the age of 4 months; fiber bundle loss is illustrated by the broken black lines.

communications between RGCs and post-synaptic neurons within the visual cortex. Therefore, to enable an accurate response to visual stimuli, the transmission of visual information requires functional RGCs. In *Hq* mice, the disappearance of RGCs begins by the age of 3 months, and 3 months later the number of RGCs is approximately half of the number present in control mice (Fig. 5 and Table 5). The ONs of *Hq* mice aged 8–10 months display severe respiratory chain dysfunction, particularly of complex I and IV (Fig. 8) which lead to a significant reduction of ATP levels within RGC axons. Thus, deleterious consequences for axonal transport/dendritic integrity can occur and pave the way for an irreversible loss of visual function. Gene therapy targeting RGCs, as carried out in this study, aimed to preserve respiratory chain functionality by increasing the amounts of Aif or neuroglobin in the retinas of *Hq* mice in which RGC degeneration had already begun. In the other hand, astrocytes and Müller cells are the major glial cells in normal retina; they maintain the blood-retina barrier and RGC health. Moreover, Müller cells protect neurons after retinal injury, *via* glutamate uptake, neovascularization facilitation, and the release of neurotrophic factors or

free-radical scavengers. In response to retinal damage, glial cells lose their physiologic functions and exhibit a reactive phenotype, which is characterized by the accumulation of GFAP and expanded migration (Bringmann et al., 2006). As we found in this study, reactive gliosis is a hallmark of the pathologic process in *Hq* retinas and ONs. Remarkably, the overexpression of *Ngb* or *Aifm1* in transduced RGCs from *Hq* mice resulted in a significant attenuation of this process in both the retinas and the ONs (Figs. 5 and 8). The diminution of reactive gliosis observed in *Hq* treated mice may also be involved in the visual function preservation observed, as it has recently been described in a model of RGC injury treated with resveratrol (Luo et al., 2018).

Gene therapy also significantly improved the activity of the respiratory chain in ONs (Fig. 8). In residual RGCs, we observed preserved connections with pre-synaptic neurons at the anatomic level (Fig. 6, Table 5). The measurements of IPL thickness in retinas from treated and untreated *Hq* mice indicated that the axonal/dendritic terminals and the overall synaptic circuitries of RGCs in retinas of treated *Hq* mice had been preserved. The rescue from the width reduction of the IPL suggested that there was some plasticity in the inner retina (Fig. 7), which could lead to the reintegration of RGC axons into appropriates visual circuitries in the retina and the visual cortex (Fig. 9). This was confirmed by recording since treated *Hq* mice exhibited improved visual cortex activity. F-VEP measurement is considered a quantitative assessment of the visual pathway from the retina to the visual cortex. N1 and P1 peaks are produced by retino-geniculate fibers, which are the principal connections between the ONs and the occipital cortex. When RGC function is diminished, the sensory input after light stimulation is unable to reach the visual cortex (Siu and Morley, 2008; Gidday et al., 2015). Despite the small number of RGCs remaining in treated *Hq* mice (Fig. 5, Table 5), they could elicit enhanced visual cortex activity (Fig. 9). Psychophysical measurements of visual acuity corroborated the preservation of visual information transmission to the visual cortex by the residual RGCs; indeed, treated eyes exhibited a significant increase in spatial visual sensitivity (Fig. 10). Thus, the collective morphologic and functional findings in treated retinas of *Hq* mice are reminiscent of anatomic hallmarks described by Park and colleagues, who demonstrated changes in the inner retinal layers corresponding to newly made connections between RGCs and bipolar cells and the extension of RGC dendrites as an early response to elevated intraocular pressure in a mouse model of glaucoma (Park et al., 2014). *Ngb* or *Aifm1* overexpression enabled improved connectivity of the circuitry in the inner retina, as evidenced in flat-mounted tissues. Morphology comparison of double-labeled β3-Tubulin and Brn3a neurons in untreated and treated *Hq* retinas showed that treated mice had 5 times more RGCs displaying better preserved dendrites relative to untreated ones (Fig. 6, Table 5). These RGCs with apparent preserved connections in inner retinas and theirs axons which have a better bioenergetics status could contribute to an enhanced visual cortex activity leading to positive consequences for visual function in *Hq* mice.

In spite of gene therapy efficacy regarding RGC morphology and function the improvement of visual function was incomplete. Several reasons can be evoked: (a) only one eye was subjected to gene therapy; (b) *Hq* mice aged about six months loss approximately half of photoreceptors which are marginally transduced when vectors are administered in the vitreous body; (c) The almost complete depletion of Aif has certainly deleterious consequences for the visual system as a whole and in the present study gene therapy was restricted to RGCs. The functionality of the optic nerve regarding the transmission of the electrical inputs from RGCs in the inner retina to the brain involved astrocytes and oligodendrocytes which were not transduced by our procedure. To achieve the optimization of the biological benefit for visual function in *Hq* mice, it is crucial to treat simultaneously photoreceptors, CGRs, oligodendrocytes, astrocytes and neurons of the visual cortex. In adult mice, this is feasible by administrating the vectors into the vein of the retro-orbital sinus (systemic delivery) (Challis et al., 2019) but this is beyond the scope of the present study.

Two main conclusions can be drawn from this study: (1) Subjecting *Hq* mice to gene therapy with AAV2/2-*Ngb* or AAV2/2-*Aifm1* when optic nerve degeneration has reached an advanced stage enables the functional recovery of the surviving RGCs, through the restoration of their bioenergetics status. Hence, the reintegration of their axons into the appropriate visual circuitries inside the retina and the visual cortex significantly reduces the extent of visual function impairment; (2) Despite no overlapping functions between the Aif and neuroglobin proteins have been identified to date, *Ngb*-mediated gene therapy was sufficient to bypass the absence of Aif in *Hq* retinas, efficiently preventing the bioenergetics crisis in RGCs, thereby leading to improved visual function.

This study did not identify the precise molecular mechanism responsible for neuroglobin action, nevertheless histochemical studies showed that both Ngb and Aif localize to mitochondria. Further, battery of experiments gathers strong evidence for the presence of the Ngb inside the mitochondria: (a) the *in situ* PLA assay allowed to unequivocally evidence that Aif and Ngb are within 40 nm distance from each other inside the organelle which should facilitate their shared physiological functions. Besides, interactions between Ngb and the mitochondrial proteins CytC (hemoprotein interacting with both Complex III and IV), Vdac which is responsible for the transport of most respiratory substrates and considered as a master regulator of the organelle bioenergetics (Fang and Maldonado, 2018) and subunit β of the ATP synthase (Complex V) were evidenced with the *in situ* PLA assay in retinas corroborating the fact that Ngb localizes to mitochondria and interacts with an array of partners within the organelle (Figs. 4B, S3 S4 and S5). Interactions between Ngb and CytC or Vdac have been evidenced in primary cultures of cortical neurons (Yu et al., 2012a), (Yu et al., 2013b). Comparative protein interactomics of primary hippocampal neurons from young mice evidenced that either the subunit β of the ATP synthase or Aif interact with Ngb, under hypoxic conditions (Haines et al., 2012).

Moreover, biochemical isolation of crude mitochondrial fractions and mitoplasts (vesicles encompassing the mitochondrial matrix and inner membrane) from mouse retina demonstrated that Ngb is mostly located inside the mitochondria at the same proportion that the known mitochondrial proteins Opa1, Ndufa9, Aif, ATP synthase (subunit β), Aif, and Tomm20 (Supplemental Fig. 6). Definitively, the biochemical and morphological evidences shown here demonstrate that Ngb is strongly connected with mitochondrial proteins which could account for its role in protecting the bioenergetics status of retinal neurons in *Harlequin* mice.

Therefore, *Ngb* overexpression may represent an innovative therapeutic strategy leading to the protection of mitochondrial function regardless of the mutation responsible for the disease; both in the context of primary mitochondrial diseases caused by mutations in mitochondrial genes, which to date are incurable (Russell et al., 2020; Zhang et al., 2020) and neurologic disorders in which the symptoms are aggravated as a result of secondary bioenergetics failure (Monzio Compagnoni et al., 2020).

Funding

Sanofi, Ophthalmology Division-Fovea Pharmaceuticals [Grant N° L11S254], the University Pierre and Marie Curie (UPMC), the National Institute of Health and Medical Research (INSERM), the Diderot University of Paris, the National Center for Scientific Research (CNRS), LABEX LIFESENSES [Grant N° ANR-10-LABX-65] and the French Association “Ouvrir les Yeux”.

Author contributions

Designed research: H·C-T., C.L., T.D., and M.C-D.

Performed research: H·C-T., C.L., S.A., V.M-B., E.R., G.LG., J.D., M.S., and M.C-D.

Analyzed data: H·C-T., S.A., C.L., J.D., M.S., V.M-B., G.LG., E.R., T.D., and M.C-D.

Wrote the paper: H·C-T., C.L., V.M-B., and M.C-D.

Availability of data and materials

The datasets during and/or analyzed during the current study available from the corresponding author on reasonable request.

Consent for publication

Not applicable.

Declaration of competing interest

T.D. was employed by Sanofi Fovea—Ophthalmology, which supported the study between 2012 and 2016; he is still working at Sanofi (Business Development & Licencing, Sanofi Partening). An international application for a patent has been filed on neuroglobin (Patent PCT/EP2014/070991 and EP3052124A1). The authors have no other patents, marketed products, or products in development to declare.

Acknowledgments

We are grateful to Stéphane Fouquet and Marie-Laure Niepon (Imaging Facility of the Vision Institute), Zsolt Csaba (Microscopy and Imaging Platforms of the NeuroDiderot laboratory), Pr. Jose-Alain Sahel (Vision Institute Director, Paris France) and Pr. Pierre Gressens (Director of the NeuroDiderot laboratory, Paris France). The authors acknowledge Margaux Le for her technical assistance during her internship of her undergraduate studies (University de Paris). We also thank Keith A. Laycock (St. Jude Children's Research Hospital) for editing the manuscript.

Appendix A. Supplementary data

Supplementary data to this article can be found online at https://doi.org/10.1016/j.nbd.2021.105483.

References

Ascenzi, P., et al., 2016. Neuroglobin: from structure to function in health and disease. Mol. Asp. Med. 52, 1–48.
Baez-Jurado, E., et al., 2018. Mitochondrial neuroglobin is necessary for protection induced by conditioned medium from human adipose-derived mesenchymal stem cells in astrocytic cells subjected to scratch and metabolic injury. Mol. Neurobiol. 56, 5167–5187.
Benit, P., et al., 2006. Three spectrophotometric assays for the measurement of the five respiratory chain complexes in minuscule biological samples. Clin. Chim. Acta 374, 81–86.
Bernard-Marissal, N., et al., 2018. Endoplasmic reticulum and mitochondria in diseases of motor and sensory neurons: a broken relationship? Cell Death Dis. 9, 333.
Biousse, V., Newman, N.J., 2017. Diagnosis and clinical features of common optic neuropathies. Lancet Neurol. 15, 1355–1367.
Bouaita, A., et al., 2012. Downregulation of apoptosis-inducing factor in Harlequin mice induces progressive and severe optic atrophy which is durably prevented by AAV2-AIF1 gene therapy. Brain. 135, 35–52.
Bringmann, A., et al., 2006. Muller cells in the healthy and diseased retina. Prog. Retin. Eye Res. 25, 397–424.
Burmester, T., et al., 2000. A vertebrate globin expressed in the brain. Nature. 407, 520–523.
Carelli, V., et al., 2017. Optic neuropathies: the tip of the neurodegeneration iceberg. Hum. Mol. Genet. 26, R139–R150.
Chakraborty, S., et al., 2018. Mitochondria in health and disease. Mitochondrion. 43, 25–29. https://doi.org/10.1016/j.mito.2018.06.006.
Challis, R.C., et al., 2019. Systemic AAV vectors for widespread and targeted gene delivery in rodents. Nat. Protoc. 14, 379–414.
Chen, X., et al., 2015. Long-term neuroglobin expression of human astrocytes following brain trauma. Neurosci. Lett. 606, 194–199.
Cuenca, N., et al., 2014. Cellular responses following retinal injuries and therapeutic approaches for neurodegenerative diseases. Prog. Retin. Eye Res. 43, 17–75.
Cwerman-Thibault, H., et al., 2015. Nuclear expression of mitochondrial ND4 leads to the protein assembling in complex I and prevents optic atrophy and visual loss. Mol. Ther. Methods Clin. Dev. 2, 15003.
Cwerman-Thibault, H., et al., 2017. Neuroglobin can prevent or reverse glaucomatous progression in DBA/2J mice. Mol. Ther. Methods Clin. Dev. 5, 200–220.
Davison, J.E., Rahman, S., 2017. Recognition, investigation and management of mitochondrial disease. Arch. Dis. Child. 102, 1082–1090.
Del Dotto, V., et al., 2018. Eight human OPA1 isoforms, long and short: what are they for? Biochim. Biophys. Acta Bioenerg. 1859, 263–269.
Dordea, A.C., et al., 2016. An open-source computational tool to automatically quantify immunolabeled retinal ganglion cells. Exp. Eye Res. 147, 50–56.
Douglas, R.M., et al., 2005. Independent visual threshold measurements in the two eyes of freely moving rats and mice using a virtual-reality optokinetic system. Vis. Neurosci. 22, 677–684.
Fang, D., Maldonado, E.N., 2018. VDAC regulation: a mitochondrial target to stop cell proliferation. Adv. Cancer Res. 138, 41–69.
Fernandez-Vizarra, E., Zeviani, M., 2021. Mitochondrial disorders of the OXPHOS system. FEBS Lett. 595, 1062–1106.
Formosa, L.E., et al., 2018. Building a complex complex: assembly of mitochondrial respiratory chain complex I. Semin. Cell Dev. Biol. 76, 154–162.
Gidday, J.M., et al., 2015. Enhanced retinal ganglion cell survival in glaucoma by hypoxic postconditioning after disease onset. Neurotherapeutics 12, 502–514.
Golpich, M., et al., 2016. Mitochondrial dysfunction and biogenesis in neurodegenerative diseases: pathogenesis and treatment. CNS Neurosci. Ther. 23, 5–22.
Gorman, G.S., et al., 2015. Prevalence of nuclear and mitochondrial DNA mutations related to adult mitochondrial disease. Ann. Neurol. 77, 753–759.
Gruosso, F., et al., 2021. Therapeutical management and drug safety in mitochondrial diseases-update 2020. J. Clin. Med. 10.
Haines, B.A., et al., 2012. Comparative protein interactomics of neuroglobin and myoglobin. J. Neurochem. 123, 192–198.
Hegazy, M., et al., 2020. Proximity ligation assay for detecting protein-protein interactions and protein modifications in cells and tissues in situ. Curr. Protoc. Cell. Biol. 89, e115.
Hellstrom, M., et al., 2009. Cellular tropism and transduction properties of seven adeno-associated viral vector serotypes in adult retina after intravitreal injection. Gene Ther. 16, 521–532.
Herrera, E., et al., 2019. Cranial pair II: the optic nerves. Anat. Rec. (Hoboken) 302, 428–445.
Hippert, C., et al., 2015. Muller glia activation in response to inherited retinal degeneration is highly varied and disease-specific. PLoS One 10, e0120415.
Hundahl, C.A., et al., 2010. Anatomical characterization of cytoglobin and neuroglobin mRNA and protein expression in the mouse brain. Brain Res. 1331, 58–73.
Ito, Y.A., Di Polo, A., 2017. Mitochondrial dynamics, transport, and quality control: a bottleneck for retinal ganglion cell viability in optic neuropathies. Mitochondrion. 36, 186–192.
Jammoul, F., et al., 2009. Taurine deficiency is a cause of vigabatrin-induced retinal phototoxicity. Ann. Neurol. 65, 98–107.
Jayaraman, T., et al., 2011. 14-3-3 binding and phosphorylation of neuroglobin during hypoxia modulate six-to-five heme pocket coordination and rate of nitrite reduction to nitric oxide. J. Biol. Chem. 286, 42679–42689.
Jiang, S.M., et al., 2015. beta-III-tubulin: a reliable marker for retinal ganglion cell labeling in experimental models of glaucoma. Int. J. Ophthalmol. 8, 643–652.
Johnson Jr., J.E., et al., 2007. Spatiotemporal regulation of ATP and Ca2+ dynamics in vertebrate rod and cone ribbon synapses. Mol. Vis. 13, 887–919.
Kay, C.N., et al., 2013. Targeting photoreceptors via intravitreal delivery using novel, capsid-mutated AAV vectors. PLoS One 8, e62097.
Klein, J.A., et al., 2002. The harlequin mouse mutation downregulates apoptosis-inducing factor. Nature. 419, 367–374.
Krasnikov, B.F., et al., 2005. Transglutaminase activity is present in highly purified nonsynaptosomal mouse brain and liver mitochondria. Biochemistry 44, 7830–7843.
Lechauve, C., et al., 2012. Neuroglobin involvement in respiratory chain function and retinal ganglion cell integrity. Biochim. Biophys. Acta 1823, 2261–2273.
Lechauve, C., et al., 2014. Neuroglobin gene therapy prevents optic atrophy and preserves durably visual function in harlequin mice. Mol. Ther. 22, 1096–1109.
Luo, H., et al., 2018. Resveratrol delays retinal ganglion cell loss and attenuates gliosis-related inflammation from ischemia-reperfusion injury. Invest. Ophthalmol. Vis. Sci. 59, 3879–3888.
Makowiecki, K., et al., 2015. Reliability of VEP recordings using chronically implanted screw electrodes in mice. Transl. Vis. Sci. Technol. 4, 15.
Matsunaga, Y., et al., 2012. Visual functional and histopathological correlation in experimental autoimmune optic neuritis. Invest. Ophthalmol. Vis. Sci. 53, 6964–6971.
Mead, B., Tomarev, S., 2016. Evaluating retinal ganglion cell loss and dysfunction. Exp. Eye Res. 151, 96–106.
Modesti, L., et al., 2021. Mitochondrial Ca(2+) signaling in health, disease and therapy. Cells. 10.
Monzio Compagnoni, G., et al., 2020. The role of mitochondria in neurodegenerative diseases: the lesson from Alzheimer's disease and Parkinson's disease. Mol. Neurobiol. 57, 2959–2980.
Nadal-Nicolas, F.M., et al., 2012. Whole number, distribution and co-expression of brn3 transcription factors in retinal ganglion cells of adult albino and pigmented rats. PLoS One 7, e49830.
Neveu, M.M., Jeffery, G., 2007. Chiasm formation in man is fundamentally different from that in the mouse. Eye (Lond). 21, 1264–1270.

Noble, J.W., et al., 2016. Loukoumasomes are distinct subcellular structures from rods and rings and are structurally associated with MAP2 and the nuclear envelope in retinal cells. PLoS One 11, e0165162.
Pang, J.J., Wu, S.M., 2011. Morphology and immunoreactivity of retrogradely double-labeled ganglion cells in the mouse retina. Invest. Ophthalmol. Vis. Sci. 52, 4886–4896.
Paques, M., et al., 2006. High resolution fundus imaging by confocal scanning laser ophthalmoscopy in the mouse. Vis. Res. 46, 1336–1345.
Park, H.Y., et al., 2014. Alterations of the synapse of the inner retinal layers after chronic intraocular pressure elevation in glaucoma animal model. Mol. Brain 7, 53.
Pass, T., et al., 2021. Selective neuron vulnerability in common and rare diseases-mitochondria in the focus. Front. Mol. Biosci. 8, 676187.
Pilz, Y.L., et al., 2017. A review of mitochondrial optic neuropathies: from inherited to acquired forms. J. Opt. 10, 205–214.
Prusky, G.T., et al., 2004. Rapid quantification of adult and developing mouse spatial vision using a virtual optomotor system. Invest. Ophthalmol. Vis. Sci. 45, 4611–4616.
Raefsky, S.M., Mattson, M.P., 2017. Adaptive responses of neuronal mitochondria to bioenergetic challenges: roles in neuroplasticity and disease resistance. Free Radic. Biol. Med. 102, 203–216.
Reyes, A., et al., 2011. Actin and myosin contribute to mammalian mitochondrial DNA maintenance. Nucleic Acids Res. 39, 5098–5108.
Ridder 3rd, W.H., Nusinowitz, S., 2006. The visual evoked potential in the mouse–origins and response characteristics. Vis. Res. 46, 902–913.
Russell, O.M., et al., 2020. Mitochondrial diseases: hope for the future. Cell 181 (1), 168–188. https://doi.org/10.1016/j.cell.2020.02.051.
Ruzzenente, B., et al., 2016. Mouse models for mitochondrial diseases. Hum. Mol. Genet. 25, R115–R122.
Sakagami, H., et al., 2017. BRAG2a, a guanine nucleotide exchange factor for Arf6, is a component of the dystrophin-associated glycoprotein complex at the photoreceptor terminal. Invest. Ophthalmol. Vis. Sci. 58, 3795–3803.
Salinas-Navarro, M., et al., 2009. A computerized analysis of the entire retinal ganglion cell population and its spatial distribution in adult rats. Vis. Res. 49, 115–126.
Schlamp, C.L., et al., 2013. Evaluation of the percentage of ganglion cells in the ganglion cell layer of the rodent retina. Mol. Vis. 19, 1387–1396.
Singh, A., et al., 2019. Oxidative stress: a key modulator in neurodegenerative diseases. Molecules. 24.
Siu, T.L., Morley, J.W., 2008. Suppression of visual cortical evoked responses following deprivation of pattern vision in adult mice. Eur. J. Neurosci. 28, 484–490.
Takahashi, K., et al., 2018. In vitro rejuvenation of brain mitochondria by the inhibition of actin polymerization. Sci. Rep. 8, 15585.
Tanimoto, N., et al., 2013. Functional phenotyping of mouse models with ERG. Methods Mol. Biol. 935, 69–78.
Tejero, J., 2020. Negative surface charges in neuroglobin modulate the interaction with cytochrome c. Biochem. Biophys. Res. Commun. 523, 567–572.
Thompson, K., et al., 2020. Recent advances in understanding the molecular genetic basis of mitochondrial disease. J. Inherit. Metab. Dis. 43 (1), 36–50. https://doi.org/10.1002/jimd.12104.
Tian, N., 2012. Development of Retinal Ganglion Cell Dendritic Structure and Synaptic Connections.
Vahsen, N., et al., 2004. AIF deficiency compromises oxidative phosphorylation. EMBO J. 23, 4679–4689.
Van Acker, Z.P., et al., 2018. Neuroglobin expression in the brain: a story of tissue homeostasis preservation. Mol. Neurobiol. 56 (3), 2101–2122. https://doi.org/10.1007/s12035-018-1212-8.
Van Acker, Z.P., et al., 2019. Connecting the dots in the neuroglobin-protein interaction network of an unstressed and ferroptotic cell death neuroblastoma model. Cells. 8.
Venit, T., et al., 2020. A dynamic actin-dependent nucleoskeleton and cell identity. J. Biochem. 169, 243–257.
Wanders, R.J.A., et al., 2020. Mitochondrial fatty acid oxidation disorders: laboratory diagnosis, pathogenesis, and the complicated route to treatment. J. Lipid Atheroscler. 9, 313–333.
Wang, R., et al., 2017. Astrocytes in the optic nerve head of glaucomatous mice display a characteristic reactive phenotype. Invest. Ophthalmol. Vis. Sci. 58, 924–932.
Weis, B.L., et al., 2013. Protein targeting to subcellular organelles via MRNA localization. Biochim. Biophys. Acta 1833, 260–273.
Xie, X., et al., 2018. In mitochondria beta-actin regulates mtDNA transcription and is required for mitochondrial quality control. iScience 3, 226–237.
Yu, Z., et al., 2012a. Identification of neuroglobin-interacting proteins using yeast two-hybrid screening. Neuroscience 200, 99–105. https://doi.org/10.1016/j.neuroscience.2011.10.046.
Yu, Z., et al., 2012b. Mitochondrial distribution of neuroglobin and its response to oxygen-glucose deprivation in primary-cultured mouse cortical neurons. Neuroscience 218, 235–242.
Yu, D.Y., et al., 2013a. Retinal ganglion cells: energetics, compartmentation, axonal transport, cytoskeletons and vulnerability. Prog. Retin. Eye Res. 36, 217–246.
Yu, Z., et al., 2013b. Neuroglobin overexpression inhibits oxygen-glucose deprivation-induced mitochondrial permeability transition pore opening in primary cultured mouse cortical neurons. Neurobiol. Dis. 56, 95–103.
Zanna, C., et al., 2008. OPA1 mutations associated with dominant optic atrophy impair oxidative phosphorylation and mitochondrial fusion. Brain 131, 352–367.
Zhang, L., et al., 2020. Advances in drug therapy for mitochondrial diseases. Ann. Transl. Med. 8, 17.